IEEE Access
Multidisciplinary | Rapid Review | Open Access Journal

Received June 19, 2020, accepted August 7, 2020, date of publication August 10, 2020, date of current version August 21, 2020.

Digital Object Identifier 10.1109/ACCESS.2020.3015614

Frequency-Coupled Impedance Modeling and Resonance Analysis of DFIG-Based Offshore Wind Farm With HVDC Connection

YONGGANG ZHANG, (Graduate Student Member, IEEE), CHRISTIAN KLABUNDE, (Member, IEEE), AND MARTIN WOLTER, (Senior Member, IEEE)

Institute of Electric Power Systems, Otto von Guericke University Magdeburg, 39106 Magdeburg, Germany

Corresponding author: Yonggang Zhang (yonggang.zhang@ovgu.de)

This work was supported by the China Scholarship Council (CSC) under Grant 201608320229.

ABSTRACT Motivated by recent years' resonance incidents in wind-integrated power systems, this paper investigates the resonance-induced harmonic distortion and stability issues in doubly fed induction generator (DFIG)-based offshore wind farm (OWF) with high-voltage direct current (HVDC) grid connection. To accurately capture the dynamic characteristics of DFIG-based wind farm, a comprehensive impedance modelling considering the detailed PI control loop and DC dynamics of wind turbine as well as the cable connections of the medium-voltage (MV) collector system is conducted. Through stepwise simulation verifications, aggregated modelling of MV collector system is proved to be suitable for wideband resonance analysis. On this basis, the resonance analysis regarding grid topology change and controller parameter variation is conducted and the impact of frequency coupling on subsynchronous resonance (SSR), middle- and high-frequency resonances is analyzed using the aggregated models derived from a practical HVDC connected DFIG-based OWF. The strength or degree of the frequency coupling between the sequence impedances of wind farm, which is induced by the asymmetrical converter control of wind turbines, is found to be dependent on the impedances of all the components of the system. Moreover, case studies are conducted to demonstrate the importance of including the frequency coupling in SSR stability assessment. Simulations in MATLAB / Simulink validate the modelling and resonance analysis.

INDEX TERMS Aggregated modelling, doubly fed induction generator (DFIG), medium-voltage (MV) collector system, wind farm, resonance analysis, HVDC.

I. INTRODUCTION

Over the last decade, many offshore wind farms (OWF) have been developed and integrated into grids through high-voltage direct current (HVDC) transmissions in the North and Baltic Seas. The interactions among wind turbines (WTs), HVDC converters and passive grid components can introduce a variety of inductive-capacitive (LC) resonances. The stimulation of such resonances may amplify harmonic distortions to a level that violates the recommended limit values as given in IEEE Std. 519-2014 [1] or induce oscillation instability when the damping of a resonance mode is quite small or negative [2]. The consequences of the resonance problems can be the blocking of HVDC converter, trip-out of WTs or the destruction of grid assets, as reported in [3]–[5]. Identification and mitigation of such resonances under all possible operating conditions and grid configurations is becoming essential for power system operators [6].

On the resonances in wind-integrated power systems, the sub-synchronous resonance (SSR), middle- and high-frequency resonances (typically at the frequency range from one or several hundred Hz to a few kHz) between DFIG-based wind farm and AC grids, as well as the SSR between full-converter based wind farm and HVDC system have been intensively studied in recent years [7]–[13]. The used AC grids are usually series-compensated grid or weak grid. Additionally, the resonances between DFIG-based OWF and HVDC grid connection are investigated in [2], [14]–[16].

The associate editor coordinating the review of this manuscript and approving it for publication was Ali Raza.

However, all the above studies that are related to DFIG-based WT have at least one of the following model simplifications: (1) simplified DFIG impedance model ignoring the converter outer loop control and DC side dynamics; (2) simple single-machine wind farm model without considering the internal cable connections; (3) aggregated wind farm model neglecting the capacitance effect of the collecting cables. These modeling simplifications made to DFIG-based wind farm are not in favorable of the accurate identification of the resonances in the large-scale DFIG-based OWF with tens of widely distributed WTs.

As for the impedance modelling of DFIG-based WT, most recent publications either have not incorporated the detailed double-loop PI control or neglect the DC side dynamics [17]–[19], which makes them incapable of capturing the exact low-frequency impedance responses of DFIG-based wind energy conversion system [20]. Additionally, the frequency coupling between the sequence impedances of DFIG-based WT are often neglected in stability analysis [2], [21], [22], which can lead to wrong judgement in the assessment of SSR stability [18], [20]. In order to accurately evaluate the risks of resonances for a wide frequency range, this paper derives a detailed impedance model of DFIG-based WT taking into account of all relevant control dynamics. Unlike the impedance model derived in [20], where the dq frame impedances are linearly transformed to modified sequence impedances, as defined in [23], this paper transforms the dq frame impedances to the real sequence impedances through both linear transformation and frequency shifting. Moreover, the more commonly applied outer-loop control with rotor speed PI controller [24], [25] instead of active power PI controller [20] is adopted in this paper.

Regarding the large number of WTs in modern OWFs, aggregated single-machine model is usually used in resonance analysis, and the most widely used aggregation model is based on the equivalent power loss or voltage drop aggregation technique [26], [27]. For a wind farm with tens of WTs, the wideband impedance characteristic of the wind farm can hardly be directly measured in simulation due to the huge computational burden, thus can rarely be used to validate the aggregated single-machine model. To tackle this issue, a stepwise simulation validation approach is proposed to check whether aggregated single-machine model is suitable for wideband resonance analysis.

Based on the detailed impedance modeling of DFIG-based WT and the aggregated modelling of medium-voltage (MV) collector system, this paper furtherly analyzes the resonances in the frequency-coupled multi-input multi-output (MIMO) system using the equivalent single-input single-output (SISO) sequence component systems. The nodal impedances at the point of common coupling (PCC) for wind farm and HVDC transmission are used to identify the critical resonance modes and evaluate the risk of oscillation stability and amplification of harmonic distortions. The impact of the frequency coupling between the sequence impedances of the DFIG-based OWF on SSR, middle- and high-frequency resonances are analyzed considering grid topology change and controller parameter variation.

The rest of this paper is organized as follows: Section II presents the dq-domain impedance modelling of DFIG-based WT and its transformation to sequence domain impedances. Section III follows with the aggregated modelling of wind farm MV collector system and the assessment of its suitability for wideband resonance analysis. Section IV addresses the resonance issues observed between DFIG-based OWF and HVDC transmission through cases studies. Section V presents the simulation validation of modelling and resonance analysis and section VI concludes the work.

II. IMPEDANCE MODELLING OF DFIG-BASED WIND TURBINE

Figure 1 shows the circuit and control diagram of the investigated DFIG-based WT, which is comprised of an induction machine, a rotor side converter (RSC) and a grid side converter (GSC). Cascaded double-loop PI control in synchronous reference frame (SRF) is adopted for both the GSC and RSC. The RSC controls the active power of the generator through regulating the rotor speed in the d-axis control loop and controls the reactive power or the AC voltage of the WT in the q-axis control loop. The GSC controls the DC side voltage. Phase-locked loop is used to synchronize the terminal voltage of the WT with grid voltage.

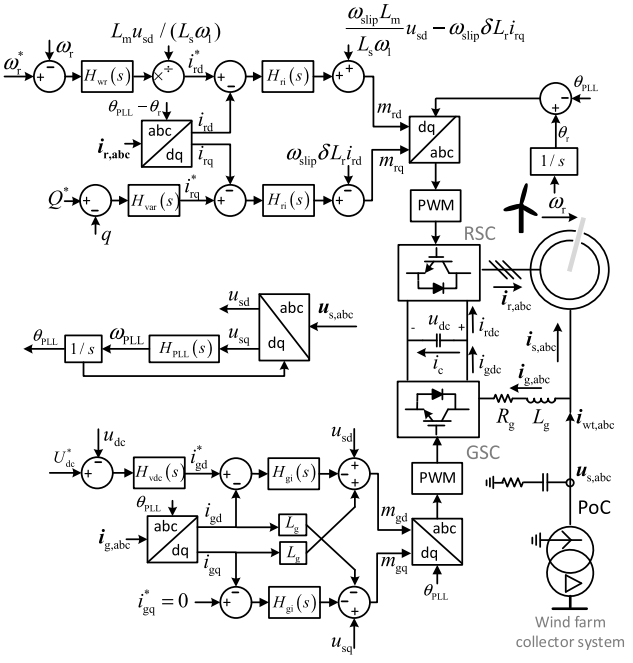

FIGURE 1. Circuit and control diagram of the investigated DFIG-based wind turbine.

Since the converter control is implemented in SRF, the impedance modelling of the DFIG-based WT will be firstly conducted in dq frame, and then for easier simulation validation and application in resonance analysis, it is transformed to sequence domain. According to the dq frame current and voltage relationships as illustrated in Figure 1,

the frequency domain representation of the DFIG energy conversion system are easily found to be

$$\begin{aligned}
&\text{GSC Branch}\begin{cases}\Delta\underline{\boldsymbol{i}}_{\mathrm{g,dq}}=\underline{\boldsymbol{Y}}_{\mathrm{gsc}}\Delta\underline{\boldsymbol{u}}_{\mathrm{s,dq}}-\underline{\boldsymbol{a}}_{2\times1}\Delta\underline{u}_{\mathrm{dc}}\\ \Delta\underline{i}_{\mathrm{gdc}}=\underline{\boldsymbol{b}}_{1\times2}\Delta\underline{\boldsymbol{u}}_{\mathrm{s,dq}}-\underline{Y}_{\mathrm{gdc}}\Delta\underline{u}_{\mathrm{dc}}\end{cases}\\
&\text{RSC Branch}\begin{cases}\Delta\underline{\boldsymbol{i}}_{\mathrm{s,dq}}=\underline{\boldsymbol{Y}}_{\mathrm{rsc}}\Delta\underline{\boldsymbol{u}}_{\mathrm{s,dq}}+\underline{\boldsymbol{c}}_{2\times1}\Delta\underline{u}_{\mathrm{dc}}\\ \Delta\underline{i}_{\mathrm{rdc}}=\underline{\boldsymbol{d}}_{1\times2}\Delta\underline{\boldsymbol{u}}_{\mathrm{s,dq}}+\underline{Y}_{\mathrm{rdc}}\Delta\underline{u}_{\mathrm{dc}}\end{cases}\\
&\text{DC Link}\quad C_{\mathrm{dc}}s\Delta\underline{u}_{\mathrm{dc}}=\Delta\underline{i}_{\mathrm{gdc}}-\Delta\underline{i}_{\mathrm{rdc}}
\end{aligned}\tag{1}$$

where the symbol Δ denotes small signal perturbation or response, the voltage and current variables in bold type denote the d- and q-axis component vectors, e.g. $\Delta\underline{\boldsymbol{u}}_{\mathrm{s,dq}}=[\Delta\underline{u}_{\mathrm{sd}}\Delta\underline{u}_{\mathrm{sq}}]^{\mathrm{T}}$, the other quantities in bold type are matrices, column or row vectors, and the underlined quantities denote complex values. The basic idea of the dq-frame impedance modelling as given in (1) is: when imposing a voltage perturbation $\Delta\underline{\boldsymbol{u}}_{\mathrm{s,dq}}$ at WT terminal, the GSC and RSC branches will have both AC current responses ($\Delta\underline{\boldsymbol{i}}_{\mathrm{g,dq}}$ and $\Delta\underline{\boldsymbol{i}}_{\mathrm{s,dq}}$) and DC current responses ($\Delta\underline{i}_{\mathrm{gdc}}$ and $\Delta\underline{i}_{\mathrm{rdc}}$), and as well, the DC link will have DC voltage response $\Delta\underline{u}_{\mathrm{dc}}$. Jointly solving the equations in (1) gives the relationship between WT terminal voltage and feed-in current, as represented by

$$\Delta\underline{\boldsymbol{i}}_{\mathrm{wt,dq}}=\Delta\underline{\boldsymbol{i}}_{\mathrm{g,dq}}+\Delta\underline{\boldsymbol{i}}_{\mathrm{s,dq}}=\underline{\boldsymbol{Y}}_{\mathrm{wt,dq}}\Delta\underline{\boldsymbol{u}}_{\mathrm{s,dq}}\tag{2}$$

where

$$\underline{\boldsymbol{Y}}_{\mathrm{wt,dq}}=\underline{\boldsymbol{Y}}_{\mathrm{gsc}}+\underline{\boldsymbol{Y}}_{\mathrm{rsc}}+\frac{\left(\underline{\boldsymbol{c}}_{2\times1}-\underline{\boldsymbol{a}}_{2\times1}\right)\left(\underline{\boldsymbol{b}}_{1\times2}-\underline{\boldsymbol{d}}_{1\times2}\right)}{\underline{Y}_{\mathrm{gdc}}+\underline{Y}_{\mathrm{rdc}}+sC_{\mathrm{dc}}}\tag{3}$$

with $\underline{\boldsymbol{Y}}_{\mathrm{wt,dq}}$ denoting WT output admittance, $\underline{\boldsymbol{Y}}_{\mathrm{gsc}}$ and $\underline{\boldsymbol{Y}}_{\mathrm{rsc}}$ denoting the output admittances of the RSC and GSC branches under the assumption of a constant DC voltage, and the other part of the admittance expression interpreting the DC-coupling of the RSC and GSC branches. Details on the derivation of the GSC and RSC models in (1) will be presented in sections II.A and II.B. Transformation of the model in (3) to sequence domain impedances will be presented in section II.C.

A. GSC BRANCH MODELLING

In the GSC branch, the converter control has two dq frames due to the dynamic of the Phase-locked Loop (PLL): one is the system dq frame (denoted by a superscript s), and another is the controller dq frame (denoted by a superscript c), as shown in Figure 2 [28]. The system dq frame is defined by the grid voltage and the controller dq frame is defined by the PLL, which estimates the frequency ω_1 and angle $\theta_1(t)$ of the grid voltage to find the position of the system dq frame. In a steady state, the controller dq frame is aligned with the system dq frame. When small-signal perturbations are added to the grid voltage, the controller dq frame is no longer aligned with the system

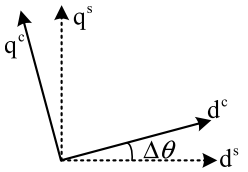

FIGURE 2. Diagram of the system and controller dq frames.

dq frame because of the PLL dynamics. The angle difference between the two dq frames is $\Delta\theta(t)=\theta_{\mathrm{PLL}}(t)-\theta_1(t)$, with $\theta_{\mathrm{PLL}}(t)$ denoting the PLL angle.

In order to deal with the nonlinearity in Park's transformation, the transformation matrix (4), as shown at the bottom of the page, can be decomposed into $\boldsymbol{T}(\theta_1(t))$ and $\boldsymbol{T}_{\Delta\theta}(t)$, as given by

$$\boldsymbol{T}\left(\theta_{\mathrm{PLL}}(t)\right)=\underbrace{\begin{bmatrix}\cos\left(\Delta\theta(t)\right) & \sin\left(\Delta\theta(t)\right)\\ -\sin\left(\Delta\theta(t)\right) & \cos\left(\Delta\theta(t)\right)\end{bmatrix}}_{\boldsymbol{T}_{\Delta\theta}(t)}\boldsymbol{T}\left(\theta_1(t)\right)\tag{5}$$

where $\boldsymbol{T}(\theta_1(t))$ denotes the Park's transformation from phase domain to the system dq frame, which equals to the rotation of $e^{-\mathrm{j}(\omega_1 t-\pi/2)}$, and $\boldsymbol{T}_{\Delta\theta}(t)$ denotes the transformation from the system dq frame to the controller dq frame. Under the assumption of a small $\Delta\theta(t)$, $\cos(\Delta\theta(t))$ can be approximated to $\Delta\theta(t)$ and $\sin(\Delta\theta(t))$ can be approximated to 1.

As the inputs of GSC control, the voltages and currents in the system dq frame need to be transformed to the controller dq frame by multiplying $\boldsymbol{T}_{\Delta\theta}(t)$. To generate the modulation signals for the power converter, the outputs of the cascaded double-loop PI control need to be transformed back to the system dq frame by multiplying $\boldsymbol{T}_{\Delta\theta}(t)^{-1}$. The frequency domain representation of the involved dq frame rotations are

$$\underline{\boldsymbol{u}}^{\mathrm{c}}_{\mathrm{s,dq}}=\underline{\boldsymbol{T}}_{\Delta\theta}\underline{\boldsymbol{u}}^{\mathrm{s}}_{\mathrm{s,dq}},\ \underline{\boldsymbol{i}}^{\mathrm{c}}_{\mathrm{g,dq}}=\underline{\boldsymbol{T}}_{\Delta\theta}\underline{\boldsymbol{i}}^{\mathrm{s}}_{\mathrm{g,dq}},\ \underline{\boldsymbol{m}}^{\mathrm{s}}_{\mathrm{g,dq}}=\underline{\boldsymbol{T}}^{-1}_{\Delta\theta}\underline{\boldsymbol{m}}^{\mathrm{c}}_{\mathrm{g,dq}}\tag{6}$$

where $\underline{\boldsymbol{T}}_{\Delta\theta}$ is the frequency domain representation of $\boldsymbol{T}_{\Delta\theta}(t)$, $\underline{\boldsymbol{u}}^{\mathrm{c}}_{\mathrm{s,dq}}=\left[\underline{u}^{\mathrm{c}}_{\mathrm{sd}}\ \underline{u}^{\mathrm{c}}_{\mathrm{sq}}\right]^{T}$, $\underline{\boldsymbol{u}}^{\mathrm{s}}_{\mathrm{s,dq}}=\left[\underline{u}^{\mathrm{s}}_{\mathrm{sd}}\ \underline{u}^{\mathrm{s}}_{\mathrm{sq}}\right]^{T}$ and other quantities follow the same notation. Performing small-signal analysis to the voltage, current and modulating signals in (6) yields

$$\begin{aligned}
\Delta\underline{\theta}&=\underline{G}_{\mathrm{PLL}}(s)\Delta\underline{u}^{\mathrm{s}}_{\mathrm{sq}}\\
\Delta\underline{\boldsymbol{u}}^{\mathrm{c}}_{\mathrm{s,dq}}&=\underline{\boldsymbol{G}}^{\mathrm{u}}_{\mathrm{PLL}}\Delta\underline{\boldsymbol{u}}^{\mathrm{s}}_{\mathrm{s,dq}},\ \Delta\underline{\boldsymbol{i}}^{\mathrm{c}}_{\mathrm{g,dq}}=\underline{\boldsymbol{G}}^{\mathrm{i}}_{\mathrm{PLL}}\Delta\underline{\boldsymbol{u}}^{\mathrm{s}}_{\mathrm{s,dq}}+\Delta\underline{\boldsymbol{i}}^{\mathrm{s}}_{\mathrm{g,dq}}\\
\Delta\underline{\boldsymbol{m}}^{\mathrm{s}}_{\mathrm{g,dq}}&=\underline{\boldsymbol{G}}^{\mathrm{m}}_{\mathrm{PLL}}\Delta\underline{\boldsymbol{u}}^{\mathrm{s}}_{\mathrm{s,dq}}+\Delta\underline{\boldsymbol{m}}^{\mathrm{c}}_{\mathrm{g,dq}}
\end{aligned}\tag{7}$$

where $\Delta\theta$ is the frequency domain representation of $\Delta\theta(t)$ and

$$\underline{G}_{\mathrm{PLL}}(s)=\frac{\underline{H}_{\mathrm{PLL}}}{s+U_{\mathrm{s1d}}\underline{H}_{\mathrm{PLL}}}\quad\underline{\boldsymbol{G}}^{\mathrm{u}}_{\mathrm{PLL}}=\begin{bmatrix}1 & U_{\mathrm{s1q}}\underline{G}_{\mathrm{PLL}}\\ 0 & 1-U_{\mathrm{s1d}}\underline{G}_{\mathrm{PLL}}\end{bmatrix}$$
$$\underline{\boldsymbol{G}}^{\mathrm{i}}_{\mathrm{PLL}}=\begin{bmatrix}0 & I_{\mathrm{g1q}}\underline{G}_{\mathrm{PLL}}\\ 0 & -I_{\mathrm{g1d}}\underline{G}_{\mathrm{PLL}}\end{bmatrix}\underline{\boldsymbol{G}}^{\mathrm{m}}_{\mathrm{PLL}}=\begin{bmatrix}0 & -M_{\mathrm{g1q}}\underline{G}_{\mathrm{PLL}}\\ 0 & M_{\mathrm{g1d}}\underline{G}_{\mathrm{PLL}}\end{bmatrix}$$

$$\boldsymbol{T}(\theta_{\mathrm{PLL}}(t))=\frac{2}{3}\begin{bmatrix}\sin\theta_{\mathrm{PLL}}(t) & \sin(\theta_{\mathrm{PLL}}(t)-2\pi/3) & \sin(\theta_{\mathrm{PLL}}(t)+2\pi/3)\\ \cos\theta_{\mathrm{PLL}}(t) & \cos(\theta_{\mathrm{PLL}}(t)-2\pi/3) & \cos(\theta_{\mathrm{PLL}}(t)+2\pi/3)\end{bmatrix}\tag{4}$$

with $\underline{H}_{\mathrm{PLL}}(s) = K_{\mathrm{pp}} + K_{\mathrm{pi}}/s$ and $U_{\mathrm{s1d}}, U_{\mathrm{s1q}}, I_{\mathrm{g1d}}, I_{\mathrm{g1q}}, M_{\mathrm{g1d}}, M_{\mathrm{g1q}}$ denoting the steady state values of the corresponding voltage, current and modulation signals. Then performing small-signal analysis to the GSC power-stage circuit and converter control yields

$$\begin{aligned}
\Delta \underline{\boldsymbol{u}}^{\mathrm{s}}_{\mathrm{s,dq}} &= \underline{\boldsymbol{Z}}_{\mathrm{RL}} \Delta \underline{\boldsymbol{i}}^{\mathrm{s}}_{\mathrm{g,dq}} + \Delta \underline{\boldsymbol{m}}^{\mathrm{s}}_{\mathrm{g,dq}} \underline{G}_{\mathrm{d}} U_{\mathrm{dc0}} + \boldsymbol{M}_{\mathrm{g1}} \underline{G}_{\mathrm{d}} \Delta \underline{u}_{\mathrm{dc}} \\
\Delta \underline{\boldsymbol{m}}^{\mathrm{c}}_{\mathrm{g,dq}} &= -\underline{\boldsymbol{G}}_{\mathrm{gi}}(s) \left(\Delta \underline{\boldsymbol{i}}^{\mathrm{ref}}_{\mathrm{g,dq}} - \Delta \underline{\boldsymbol{i}}^{\mathrm{c}}_{\mathrm{g,dq}} \right) + \boldsymbol{K}_{\mathrm{gd}} \Delta \underline{\boldsymbol{i}}^{\mathrm{c}}_{\mathrm{g,dq}} + \Delta \underline{\boldsymbol{u}}^{\mathrm{c}}_{\mathrm{s,dq}} \\
\Delta \underline{\boldsymbol{i}}^{\mathrm{ref}}_{\mathrm{g,dq}} &= -\underline{\boldsymbol{h}}_{\mathrm{vdc}} \Delta \underline{u}_{\mathrm{dc}}
\end{aligned} \tag{8}$$

where $\boldsymbol{M}_{\mathrm{g1}} = [M_{\mathrm{g1d}}\ M_{\mathrm{g1q}}]^{\mathrm{T}}$, $\underline{G}_{\mathrm{d}}(s) = 1/(1 + 1.5T_{\mathrm{s}}s)$ denotes the digital control delay for 1.5 times of sampling periods, U_{dc0} denotes the steady state value of DC voltage and

$$\begin{aligned}
\underline{\boldsymbol{Z}}_{\mathrm{RL}} &= \begin{bmatrix} R_{\mathrm{g}} + sL_{\mathrm{g}}/\omega_{\mathrm{b}} & -\omega_1 L_{\mathrm{g}} \\ \omega_1 L_{\mathrm{g}} & R_{\mathrm{g}} + sL_{\mathrm{g}}/\omega_{\mathrm{b}} \end{bmatrix} \\
\underline{\boldsymbol{G}}_{\mathrm{gi}}(s) &= \begin{bmatrix} \underline{H}_{\mathrm{gi}}(s) & 0 \\ 0 & \underline{H}_{\mathrm{gi}}(s) \end{bmatrix} \\
\boldsymbol{K}_{\mathrm{gd}} &= \begin{bmatrix} 0 & \omega_1 L_{\mathrm{g}} \\ -\omega_1 L_{\mathrm{g}} & 0 \end{bmatrix} \quad \underline{\boldsymbol{h}}_{\mathrm{vdc}} = \begin{bmatrix} \underline{H}_{\mathrm{vdc}}(s) \\ 0 \end{bmatrix}
\end{aligned}$$

with $\underline{H}_{\mathrm{gi}}(s) = K_{\mathrm{gp}} + K_{\mathrm{gi}}/s$ denoting the GSC current PI controller, $\underline{H}_{\mathrm{vdc}}(s) = K_{\mathrm{vp}} + K_{\mathrm{vi}}/s$ denoting the GSC DC voltage controller and ω_{b} is the base angular frequency for the per unit system. Jointly solving the equations in (7) and (8) yields

$$\Delta \underline{\boldsymbol{i}}^{\mathrm{s}}_{\mathrm{g,dq}} = \underline{\boldsymbol{Y}}_{\mathrm{gsc}} \Delta \underline{\boldsymbol{u}}^{\mathrm{s}}_{\mathrm{s,dq}} - \underline{\boldsymbol{a}}_{2\times 1} \Delta \underline{u}_{\mathrm{dc}} \tag{9}$$

where the detailed expression of $\underline{\boldsymbol{Y}}_{\mathrm{gsc}}$ and $\underline{\boldsymbol{a}}_{2\times 1}$ are given in Appendix A. Assuming an ideal lossless model for the converter, the time domain per unit representation of the power balance between the AC input and DC output of the GSC can be written as

$$p(t) = i_{\mathrm{gdc}}(t) u_{\mathrm{dc}}(t) = \mathrm{Re}\left\{ \underline{i}^{*}_{\mathrm{g,dq}}(t) \underline{u}_{\mathrm{g,dq}}(t) \right\} \tag{10}$$

where $\underline{i}^{*}_{\mathrm{g,dq}}(t) = i^{\mathrm{s}}_{\mathrm{gd}}(t) - \mathrm{j}i^{\mathrm{s}}_{\mathrm{gq}}(t)$ and $\underline{u}_{\mathrm{g,dq}}(t) = u^{\mathrm{s}}_{\mathrm{gd}}(t) + \mathrm{j}u^{\mathrm{s}}_{\mathrm{gq}}(t)$. Substituting $\underline{\boldsymbol{u}}_{\mathrm{g,dq}} = \underline{\boldsymbol{m}}^{\mathrm{s}}_{\mathrm{g,dq}} \underline{G}_{\mathrm{d}}$ into the frequency domain representation of (10), performing small signal analysis to and rewriting the resulted equation can give

$$\Delta \underline{i}_{\mathrm{gdc}} = \underline{G}_{\mathrm{d}} \left(\boldsymbol{M}^{\mathrm{T}}_{\mathrm{g1}} \Delta \underline{\boldsymbol{i}}^{\mathrm{s}}_{\mathrm{g,dq}} + \boldsymbol{I}^{\mathrm{T}}_{\mathrm{g1}} \Delta \underline{\boldsymbol{m}}^{\mathrm{s}}_{\mathrm{g,dq}} \right) \tag{11}$$

where $\boldsymbol{I}_{\mathrm{g1}} = [I_{\mathrm{g1d}}\ I_{\mathrm{g1q}}]^{\mathrm{T}}$. Furtherly substituting the modulating signals in (7) and (8) as well as the AC current signal in (9) into (11) yields

$$\Delta \underline{i}_{\mathrm{gdc}} = \underline{\boldsymbol{b}}_{1\times 2} \Delta \underline{\boldsymbol{u}}^{\mathrm{s}}_{\mathrm{s,dq}} - \underline{Y}_{\mathrm{gdc}} \Delta \underline{u}_{\mathrm{dc}} \tag{12}$$

where the detailed expressions of $\underline{\boldsymbol{b}}_{1\times 2}$ and $\underline{Y}_{\mathrm{gdc}}$ are given in Appendix A. Finally, the equations in (9) and (12) can represent the admittance model of the GSC branch.

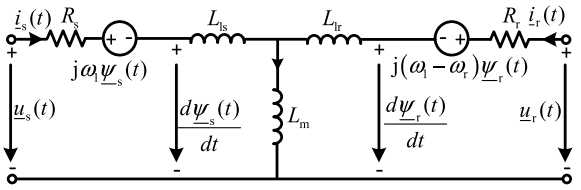

FIGURE 3. The induction machine model in system dq frame [25].

B. RSC BRANCH MODELLING

Figure 3 shows the induction machine model in system dq frame, in which all the rotor side quantities are reflected to the stator side and the variables $\underline{u}_{\mathrm{s}}(t)$, $\underline{i}_{\mathrm{s}}(t)$, $\underline{\psi}_{\mathrm{s}}(t)$, $\underline{u}_{\mathrm{r}}(t)$, $\underline{i}_{\mathrm{r}}(t)$ and $\underline{\psi}_{\mathrm{r}}(t)$ denote the space vectors composed of d- and q-axis components, e.g. $\underline{u}_{\mathrm{s}}(t) = u_{\mathrm{sd}}(t) + \mathrm{j}u_{\mathrm{sq}}(t)$.

According to relationships between the rotor and stator voltages and the rotor and stator currents as illustrated by Figure 3, their frequency domain small-signal representation can be written as

$$\begin{aligned}
\Delta \underline{\boldsymbol{u}}^{\mathrm{s}}_{\mathrm{s,dq}} &= \underbrace{\begin{bmatrix} R_{\mathrm{s}} + sL_{\mathrm{s}} & -\omega_1 L_{\mathrm{s}} \\ \omega_1 L_{\mathrm{s}} & R_{\mathrm{s}} + sL_{\mathrm{s}} \end{bmatrix}}_{\underline{\boldsymbol{Z}}_{\mathrm{ss}}} \Delta \underline{\boldsymbol{i}}^{\mathrm{s}}_{\mathrm{s,dq}} \\
&\quad + \underbrace{\begin{bmatrix} sL_{\mathrm{m}} & -\omega_1 L_{\mathrm{m}} \\ \omega_1 L_{\mathrm{m}} & sL_{\mathrm{m}} \end{bmatrix}}_{\underline{\boldsymbol{Z}}_{\mathrm{sr}}} \Delta \underline{\boldsymbol{i}}^{\mathrm{s}}_{\mathrm{r,dq}} \\
\Delta \underline{\boldsymbol{u}}^{\mathrm{s}}_{\mathrm{r,dq}} &= \underbrace{\begin{bmatrix} sL_{\mathrm{m}} & -\omega_{\mathrm{slip}} L_{\mathrm{m}} \\ \omega_{\mathrm{slip}} L_{\mathrm{m}} & sL_{\mathrm{m}} \end{bmatrix}}_{\underline{\boldsymbol{Z}}_{\mathrm{rs}}} \Delta \underline{\boldsymbol{i}}^{\mathrm{s}}_{\mathrm{s,dq}} \\
&\quad + \underbrace{\begin{bmatrix} R_{\mathrm{r}} + sL_{\mathrm{r}} & -\omega_{\mathrm{slip}} L_{\mathrm{r}} \\ \omega_{\mathrm{slip}} L_{\mathrm{r}} & R_{\mathrm{r}} + sL_{\mathrm{r}} \end{bmatrix}}_{\underline{\boldsymbol{Z}}_{\mathrm{rr}}} \Delta \underline{\boldsymbol{i}}^{\mathrm{s}}_{\mathrm{r,dq}}
\end{aligned} \tag{13}$$

where $L_{\mathrm{s}} = L_{\mathrm{ls}} + L_{\mathrm{m}}$, $L_{\mathrm{r}} = L_{\mathrm{lr}} + L_{\mathrm{m}}$ and $\omega_{\mathrm{slip}} = \omega_1 - \omega_{\mathrm{r}}$ with ω_{r} denoting the rotor speed.

In comparison with the Park's transformation of GSC control, the angle needed for the Park transformation in RSC control involves not only $\theta_{\mathrm{PLL}}(t)$, but also the angle of the rotor speed $\theta_{\mathrm{r}}(t)$. Therefore, the Park's transformation in RSC control can be decomposed into

$$\begin{aligned}
&\boldsymbol{T}\left(\theta_{\mathrm{PLL}}(t) - \theta_{\mathrm{r}}(t)\right) \\
&\quad \approx \underbrace{\begin{bmatrix} 1 & \Delta\theta(t) - \Delta\theta_{\mathrm{r}}(t) \\ -\left(\Delta\theta(t) - \Delta\theta_{\mathrm{r}}(t)\right) & 1 \end{bmatrix}}_{\boldsymbol{T}_{\Delta\theta\mathrm{r}}(t)} \\
&\quad \times \boldsymbol{T}\left(\theta_1(t) - \theta_{\mathrm{r1}}(t)\right)
\end{aligned} \tag{14}$$

where $\theta_{\mathrm{r1}}(t)$ denotes steady state value of the rotor speed angle, $\Delta\theta_{\mathrm{r}}(t) = \theta_{\mathrm{r}}(t) - \theta_{\mathrm{r1}}(t)$, $\boldsymbol{T}(\theta_1(t)\text{-}\theta_{\mathrm{r1}}(t))$ denotes the Park's transformation from the phase domain to the system dq frame and $\boldsymbol{T}_{\Delta\theta\mathrm{r}}(t)$ denotes the transformation from the system dq frame to the controller dq frame. Since the frequency domain representation of $\Delta\theta(t)$, i.e. $\Delta\theta$, is already obtained in (7), only the frequency domain representation of $\Delta\theta_{\mathrm{r}}(t)$, as defined by $\Delta\theta_{\mathrm{r}}$, is needed to get frequency domain representation of $\boldsymbol{T}_{\Delta\theta\mathrm{r}}(t)$, as defined by $\underline{\boldsymbol{T}}_{\Delta\theta\mathrm{r}}$.

For the induction machine of the wind turbine, the time domain motion, electromagnetic torque and stator voltage equations can be written as

$$\begin{aligned} \mathrm{J}\frac{d\omega_\mathrm{r}}{dt} &= T_\mathrm{m}(t) - T_\mathrm{e}(t) \\ T_\mathrm{e}(t) &= \left(\psi_\mathrm{sq}(t) i_\mathrm{rd}(t) - \psi_\mathrm{sd}(t) i_\mathrm{rq}(t)\right) L_\mathrm{m}/L_\mathrm{s} \\ &\approx \psi_\mathrm{sq}(t) i_\mathrm{rd}(t) L_\mathrm{m}/L_\mathrm{s} \\ u_\mathrm{sd}(t) &= R_\mathrm{s} i_\mathrm{sd}(t) + \frac{d\psi_\mathrm{sd}(t)}{dt} - \omega_1 \psi_\mathrm{sq}(t) \approx -\omega_1 \psi_\mathrm{sq}(t) \end{aligned} \quad (15)$$

where T_m and T_e represent the mechanical and electromagnetic torques and J is the turbine moment of inertia [25]. Performing small-signal analysis to the equations in (15) and jointly solving them in frequency domain yield

$$\Delta\underline{\omega}_\mathrm{r} = \underbrace{\frac{U_\mathrm{sd} L_\mathrm{m}}{\omega_1 L_\mathrm{s} \mathrm{J} s}}_{\underline{G}_\mathrm{wr}} \Delta\underline{i}_\mathrm{rd}, \quad \Delta\underline{\theta}_\mathrm{r} = \underbrace{\frac{U_\mathrm{sd} L_\mathrm{m}}{\omega_1 L_\mathrm{s} \mathrm{J} s^2}}_{\underline{G}_\mathrm{wtr}} \Delta\underline{i}_\mathrm{rd} \quad (16)$$

Furtherly performing small-signal analysis to the frequency domain representation of the involved dq-frame rotations in the RSC control, i.e. $\underline{\boldsymbol{i}}^\mathrm{c}_\mathrm{r,dq} = \underline{\boldsymbol{T}}_{\Delta\theta\mathrm{r}} \underline{\boldsymbol{i}}^\mathrm{s}_\mathrm{r,dq}$ and $\underline{\boldsymbol{m}}^\mathrm{s}_\mathrm{r} = \underline{\boldsymbol{T}}^{-1}_{\Delta\theta\mathrm{r}} \underline{\boldsymbol{m}}^\mathrm{c}_\mathrm{r}$, yields

$$\begin{aligned} \Delta\underline{\boldsymbol{i}}^\mathrm{c}_\mathrm{r,dq} &= \underline{\boldsymbol{G}}^\mathrm{ri}_\mathrm{PLL} \Delta\underline{\boldsymbol{u}}^\mathrm{s}_\mathrm{s,dq} + \underline{\boldsymbol{G}}^\mathrm{i}_\mathrm{wtr} \Delta\underline{\boldsymbol{i}}^\mathrm{s}_\mathrm{r,dq} \\ \Delta\underline{\boldsymbol{m}}^\mathrm{s}_\mathrm{r,dq} &= \underline{\boldsymbol{G}}^\mathrm{rm}_\mathrm{PLL} \Delta\underline{\boldsymbol{u}}^\mathrm{s}_\mathrm{s,dq} + \underline{\boldsymbol{G}}^\mathrm{m}_\mathrm{wtr} \Delta\underline{\boldsymbol{i}}^\mathrm{s}_\mathrm{r,dq} + \Delta\underline{\boldsymbol{m}}^\mathrm{c}_\mathrm{r,dq} \end{aligned} \quad (17)$$

where

$$\underline{\boldsymbol{G}}^\mathrm{ri}_\mathrm{PLL} = \begin{bmatrix} 0 & I_\mathrm{r1q}\underline{G}_\mathrm{PLL} \\ 0 & -I_\mathrm{r1d}\underline{G}_\mathrm{PLL} \end{bmatrix} \quad \underline{\boldsymbol{G}}^\mathrm{i}_\mathrm{wtr} = \begin{bmatrix} 1 - \underline{G}_\mathrm{wtr} I_\mathrm{r1q} & 0 \\ \underline{G}_\mathrm{wtr} I_\mathrm{r1d} & 1 \end{bmatrix}$$

$$\underline{\boldsymbol{G}}^\mathrm{rm}_\mathrm{PLL} = \begin{bmatrix} 0 & -M_\mathrm{r1q}\underline{G}_\mathrm{PLL} \\ 0 & M_\mathrm{r1d}\underline{G}_\mathrm{PLL} \end{bmatrix} \quad \underline{\boldsymbol{G}}^\mathrm{m}_\mathrm{wtr} = \begin{bmatrix} \underline{G}_\mathrm{wtr} M_\mathrm{r1q} & 0 \\ -\underline{G}_\mathrm{wtr} M_\mathrm{r1d} & 0 \end{bmatrix}$$

with I_r1d, I_r1q, M_r1d, M_r1q denoting the steady state values of the corresponding current and modulation signals. For the RSC control, the small-signal representation can be written as

$$\begin{aligned} \Delta\underline{\boldsymbol{u}}^\mathrm{s}_\mathrm{r} &= \Delta\underline{\boldsymbol{m}}^\mathrm{s}_\mathrm{r,dq} \underline{G}_\mathrm{d} U_\mathrm{dc0} + \boldsymbol{M}_\mathrm{r1} \underline{G}_\mathrm{d} \Delta\underline{u}_\mathrm{dc} \\ \Delta\underline{\boldsymbol{m}}^\mathrm{c}_\mathrm{r,dq} &= \underline{\boldsymbol{G}}_\mathrm{ri} \left(\Delta\underline{\boldsymbol{i}}^\mathrm{ref}_\mathrm{r,dq} - \Delta\underline{\boldsymbol{i}}^\mathrm{c}_\mathrm{r,dq}\right) + \boldsymbol{K}_\mathrm{rd} \Delta\underline{\boldsymbol{i}}^\mathrm{c}_\mathrm{r,dq} + \boldsymbol{K}_\mathrm{us} \Delta\underline{\boldsymbol{u}}^\mathrm{c}_\mathrm{s,dq} \\ \Delta\underline{\boldsymbol{i}}^\mathrm{ref}_\mathrm{r,dq} &= \underline{\boldsymbol{G}}_\mathrm{pq1} \Delta\underline{\boldsymbol{i}}^\mathrm{c}_\mathrm{r,dq} + \underline{\boldsymbol{G}}_\mathrm{var1} \Delta\underline{\boldsymbol{u}}^\mathrm{c}_\mathrm{s,dq} + \underline{\boldsymbol{G}}_\mathrm{var2} \Delta\underline{\boldsymbol{i}}^\mathrm{c}_\mathrm{s,dq} \end{aligned} \quad (18)$$

where $\boldsymbol{M}_\mathrm{r1} = [M_\mathrm{r1d}\ M_\mathrm{r1q}]^\mathrm{T}$ and

$$\underline{\boldsymbol{G}}_\mathrm{ri}(s) = \underline{H}_\mathrm{ri}(s) \begin{bmatrix} 1 & 0 \\ 0 & 1 \end{bmatrix} \quad \boldsymbol{K}_\mathrm{rd} = \begin{bmatrix} 0 & -\omega_\mathrm{slip} L_\mathrm{r} \delta \\ \omega_\mathrm{slip} L_\mathrm{r} \delta & 0 \end{bmatrix}$$

$$\boldsymbol{K}_\mathrm{us} = \begin{bmatrix} \frac{\omega_\mathrm{slip} L_\mathrm{m}}{\omega_1 L_\mathrm{s}} & 0 \\ 0 & 0 \end{bmatrix}$$

$$\underline{\boldsymbol{G}}_\mathrm{pq1} = \frac{\underline{H}_\mathrm{wr}}{\mathrm{J}s} \begin{bmatrix} 1 & 0 \\ 0 & 0 \end{bmatrix} \quad \underline{\boldsymbol{G}}_\mathrm{var1} = \underline{H}_\mathrm{var} \begin{bmatrix} 0 & 0 \\ I_\mathrm{s1q} & -I_\mathrm{s1d} \end{bmatrix}$$

$$\underline{\boldsymbol{G}}_\mathrm{var2} = \underline{H}_\mathrm{var} \begin{bmatrix} 0 & 0 \\ -U_\mathrm{s1q} & U_\mathrm{s1d} \end{bmatrix}$$

with $\underline{H}_\mathrm{ri}(s)$, $\underline{H}_\mathrm{wr}(s)$ and $\underline{H}_\mathrm{var}(s)$ denoting the RSC current PI controller, rotor speed PI controller and reactive power PI controller respectively, and $\delta = 1 - L_\mathrm{m}^2/(L_\mathrm{s}L_\mathrm{r})$ denoting the magnetic flux leakage coefficient of the induction machine. Jointly solving the equations in (13), (17) and (18) yields

$$\begin{aligned} \Delta\underline{\boldsymbol{i}}^\mathrm{s}_\mathrm{s,dq} = &\underbrace{\underline{\boldsymbol{A}}^{-1} \cdot \left\{\underline{G}_\mathrm{d} U_\mathrm{dc0} \underline{\boldsymbol{B}} - \underline{\boldsymbol{Z}}_\mathrm{rr} \underline{\boldsymbol{Z}}^{-1}_\mathrm{sr}\right\}}_{\underline{\boldsymbol{Y}}_\mathrm{rsc}} \Delta\underline{\boldsymbol{u}}^\mathrm{s}_\mathrm{s,dq} \\ &+ \underbrace{\underline{\boldsymbol{A}}^{-1} \boldsymbol{M}_\mathrm{r1} \underline{G}_\mathrm{d}}_{\underline{\boldsymbol{c}}_{2\times1}} \Delta\underline{u}_\mathrm{dc} \end{aligned} \quad (19)$$

where the detailed expressions of $\underline{\boldsymbol{A}}$ and $\underline{\boldsymbol{B}}$ are given in Appendix A. For the power balance between the AC input and DC output of the RSC, the frequency domain small-signal representation can be written as

$$\Delta\underline{i}_\mathrm{rdc} = \underline{G}_\mathrm{d} \left(\boldsymbol{M}^\mathrm{T}_\mathrm{r1} \Delta\underline{\boldsymbol{i}}^\mathrm{s}_\mathrm{r,dq} + \boldsymbol{I}^\mathrm{T}_\mathrm{r1} \Delta\underline{\boldsymbol{m}}^\mathrm{s}_\mathrm{r,dq}\right) \quad (20)$$

where $\boldsymbol{I}_\mathrm{r1} = [I_\mathrm{r1d}\ I_\mathrm{r1q}]^\mathrm{T}$. Jointly solving (17)-(20) yields

$$\Delta\underline{i}_\mathrm{rdc} = \underline{\boldsymbol{d}}_{1\times2} \Delta\underline{\boldsymbol{u}}^\mathrm{s}_\mathrm{s,dq} + \underline{Y}_\mathrm{rdc} \Delta\underline{u}_\mathrm{dc} \quad (21)$$

where the detailed expressions of $\underline{\boldsymbol{d}}_{1\times2}$ and $\underline{Y}_\mathrm{rdc}$ are given in Appendix A. Finally, the equations in (19) and (21) can represent the admittance model of the RSC and the induction machine branch.

C. DERIVATION OF WT SEQUENCE IMPEDANCES

For the convenience of model validation and grid-level resonance analysis using the phase or sequence-component quantities, the developed dq admittance model as given in (3) can be furtherly transformed to sequence impedances.

After adding small-signal perturbations to the grid voltages $\boldsymbol{u}_\mathrm{s,abc}(t)$, the phase-a voltage can be written as

$$\begin{aligned} u_\mathrm{sa}(t) = &U_1 \sin(\omega_1 t) + U_\mathrm{p} \sin\left(\omega_\mathrm{p} t + \phi_\mathrm{up}\right) \\ &+ U_\mathrm{n} \sin(\omega_\mathrm{n} t + \phi_\mathrm{un}) \end{aligned} \quad (22)$$

where the subscripts p and n denote positive and negative sequence components respectively. For the better clarification of frequency coupling, it is set $\omega_\mathrm{p} = \omega_\mathrm{n} + 2\omega_1$. After substituting the trigonometric functions in (22) with complex exponential functions, its frequency domain representation can be written as

$$\underline{U}_\mathrm{sa}(\omega) = \begin{cases} \underline{U}_1, & \omega = \pm\omega_1 \\ \underline{U}_\mathrm{p}, & \omega = \pm\omega_\mathrm{p} \\ \underline{U}_\mathrm{n}, & \omega = \pm\omega_\mathrm{n} \end{cases} \quad (23)$$

where $\underline{U}_\mathrm{p} = (U_\mathrm{p}/2) e^{\pm\mathrm{j}(\phi_\mathrm{up} - \pi/2)}$ and others follow the same notation. Then performing the Park's transformation in (4) to (23), the voltage components in system dq frame can be written as

$$\underline{U}_\mathrm{sd} = \begin{cases} \underline{U}_1, \omega_\mathrm{dq} = 0 \\ \pm\mathrm{j}\underline{U}_\mathrm{p}, \omega_\mathrm{dq} = \pm(\omega_\mathrm{p} - \omega_1) \\ \mp\mathrm{j}\underline{U}_\mathrm{n}, \omega_\mathrm{dq} = \pm(\omega_\mathrm{n} + \omega_1) \end{cases}$$

$$\underline{U}_\mathrm{sq} = \begin{cases} 0, \omega_\mathrm{dq} = 0 \\ \underline{U}_\mathrm{p}, \omega_\mathrm{dq} = \pm(\omega_\mathrm{p} - \omega_1) \\ \underline{U}_\mathrm{n}, \omega_\mathrm{dq} = \pm(\omega_\mathrm{n} + \omega_1) \end{cases} \quad (24)$$

Combining (23) and (24), the relationship between the dq components and sequence components can be solved as

$$\begin{bmatrix} \underline{U}_{\mathrm{sd}}(\omega_{\mathrm{dq}}) \\ \underline{U}_{\mathrm{sq}}(\omega_{\mathrm{dq}}) \end{bmatrix} = \underbrace{\begin{bmatrix} \mathrm{j} & -\mathrm{j} \\ 1 & 1 \end{bmatrix}}_{\boldsymbol{T}_{\mathrm{Z}}} \begin{bmatrix} \underline{U}_{\mathrm{p}}(\omega_{\mathrm{p}}) \\ \underline{U}_{\mathrm{n}}(\omega_{\mathrm{n}}) \end{bmatrix} \tag{25}$$

where the transformation matrix $\boldsymbol{T}_{\mathrm{Z}}$ also applies to the other voltage and current quantities in this study. Rewriting the equation $\Delta \underline{\boldsymbol{i}}_{\mathrm{wt,dq}} = \underline{\boldsymbol{Y}}_{\mathrm{wt,dq}} \Delta \underline{\boldsymbol{u}}_{\mathrm{s,dq}}$ in (2) for $s = \mathrm{j}\omega_{\mathrm{dq}}$ gives

$$\begin{bmatrix} \underline{U}_{\mathrm{sd}}(\omega_{\mathrm{dq}}) \\ \underline{U}_{\mathrm{sq}}(\omega_{\mathrm{dq}}) \end{bmatrix} = \underbrace{\begin{bmatrix} \underline{Z}_{\mathrm{dd}}(\omega_{\mathrm{dq}}) & \underline{Z}_{\mathrm{dq}}(\omega_{\mathrm{dq}}) \\ \underline{Z}_{\mathrm{qd}}(\omega_{\mathrm{dq}}) & \underline{Z}_{\mathrm{qq}}(\omega_{\mathrm{dq}}) \end{bmatrix}}_{\underline{\boldsymbol{Z}}_{\mathrm{wt,dq}}(\omega_{\mathrm{dq}}) = \underline{\boldsymbol{Y}}^{-1}_{\mathrm{wt,dq}}(\omega_{\mathrm{dq}})} \begin{bmatrix} \underline{I}_{\mathrm{wtd}}(\omega_{\mathrm{dq}}) \\ \underline{I}_{\mathrm{wtq}}(\omega_{\mathrm{dq}}) \end{bmatrix} \tag{26}$$

where $\underline{\boldsymbol{Z}}_{\mathrm{wt,dq}}(s)$ denotes the dq domain impedance. Then substituting the voltages and currents in (26) with the corresponding sequence components according to (25) yields

$$\begin{aligned} \begin{bmatrix} \underline{U}_{\mathrm{p}}(\omega_{\mathrm{p}}) \\ \underline{U}_{\mathrm{n}}(\omega_{\mathrm{n}}) \end{bmatrix} &= \underbrace{\boldsymbol{T}_{\mathrm{Z}}^{-1} \begin{bmatrix} \underline{Z}_{\mathrm{dd}}(\omega_{\mathrm{dq}}) & \underline{Z}_{\mathrm{dq}}(\omega_{\mathrm{dq}}) \\ \underline{Z}_{\mathrm{qd}}(\omega_{\mathrm{dq}}) & \underline{Z}_{\mathrm{qq}}(\omega_{\mathrm{dq}}) \end{bmatrix} \boldsymbol{T}_{\mathrm{Z}}}_{\substack{\underline{\boldsymbol{Z}}^{\mathrm{M}}_{\mathrm{wt,pn}}(\omega_{\mathrm{dq}}) \\ \Updownarrow \, for \; s = \mathrm{j}\omega_{\mathrm{dq}}}} \begin{bmatrix} \underline{I}_{\mathrm{p}}(\omega_{\mathrm{p}}) \\ \underline{I}_{\mathrm{n}}(\omega_{\mathrm{n}}) \end{bmatrix} \\ \begin{bmatrix} \underline{U}_{\mathrm{p}}(s+\mathrm{j}\omega_1) \\ \underline{U}_{\mathrm{n}}(s-\mathrm{j}\omega_1) \end{bmatrix} &= \underbrace{\boldsymbol{T}_{\mathrm{Z}}^{-1} \begin{bmatrix} \underline{Z}_{\mathrm{dd}}(s) & \underline{Z}_{\mathrm{dq}}(s) \\ \underline{Z}_{\mathrm{qd}}(s) & \underline{Z}_{\mathrm{qq}}(s) \end{bmatrix} \boldsymbol{T}_{\mathrm{Z}}}_{\underline{\boldsymbol{Z}}^{\mathrm{M}}_{\mathrm{wt,pn}}(s)} \\ &\quad \times \begin{bmatrix} \underline{I}_{\mathrm{p}}(s+\mathrm{j}\omega_1) \\ \underline{I}_{\mathrm{n}}(s-\mathrm{j}\omega_1) \end{bmatrix} \end{aligned} \tag{27}$$

where $\underline{\boldsymbol{Z}}^{\mathrm{M}}_{\mathrm{wt,pn}}(s) = \begin{bmatrix} \underline{Z}^{\mathrm{M}}_{\mathrm{pp}}(s) & \underline{Z}^{\mathrm{M}}_{\mathrm{pn}}(s) \\ \underline{Z}^{\mathrm{M}}_{\mathrm{np}}(s) & \underline{Z}^{\mathrm{M}}_{\mathrm{nn}}(s) \end{bmatrix}$ denotes the modified sequence-domain impedance, as defined in [23]. By shifting the frequency of ω_1 for the voltage, current and impedance terms in (27), i.e. substituting s with $s - \mathrm{j}\omega_1$ for the positive sequence and sequence coupling terms, and substituting s with $s + \mathrm{j}\omega_1$ for the negative sequence and sequence coupling terms, the real sequence-domain impedance $\underline{\boldsymbol{Z}}_{\mathrm{wt,pn}}(s)$ can be derived, which satisfies

$$\begin{bmatrix} \underline{U}_{\mathrm{p}}(s) \\ \underline{U}_{\mathrm{n}}(s) \end{bmatrix} = \underbrace{\begin{bmatrix} \underline{Z}^{\mathrm{M}}_{\mathrm{pp}}(s-\mathrm{j}\omega_1) & \underline{Z}^{\mathrm{M}}_{\mathrm{pn}}(s+\mathrm{j}\omega_1) \\ \underline{Z}^{\mathrm{M}}_{\mathrm{np}}(s-\mathrm{j}\omega_1) & \underline{Z}^{\mathrm{M}}_{\mathrm{nn}}(s+\mathrm{j}\omega_1) \end{bmatrix}}_{\underline{\boldsymbol{Z}}_{\mathrm{wt,pn}}(s)} \begin{bmatrix} \underline{I}_{\mathrm{p}}(s) \\ \underline{I}_{\mathrm{n}}(s) \end{bmatrix} \tag{28}$$

where the off-diagonal elements of $\underline{\boldsymbol{Z}}_{\mathrm{wt,pn}}(s)$ are not equal to zero and they are induced by the asymmetrical PLL control and the asymmetrical outer loop PI control of WT converters. The sequence impedance coupling in (28) reflects the relationship between the voltage and current with different frequencies. To be specific, when there is a positive-sequence current/voltage perturbation with the frequency $\omega_{\mathrm{p}} \geq 2\omega_1$, a negative-sequence voltage/current response will be induced and the frequency satisfies $\omega_{\mathrm{n}} = \omega_{\mathrm{p}} - 2\omega_1$, but if $\omega_{\mathrm{p}} < 2\omega_1$, the coupled frequency component will be in positive sequence and the frequency satisfies $\omega_{\mathrm{p2}} = 2\omega_1 - \omega_{\mathrm{p}}$.

III. IMPEDANCE MODELLING OF WIND FARM MEDIUM-VOLTAGE COLLECTOR SYSTEM

This section firstly shows the present practices in the aggregated modelling of wind farm MV collector system and then presents the suitability of the aggregated models for wideband resonance analysis through comparing them with the detailed model. Illustration of the aggregated single-machine model is given in Figure 4.

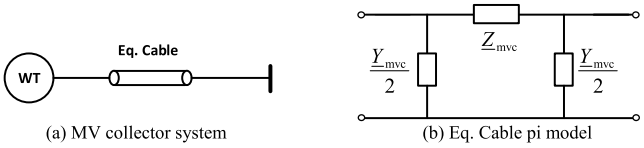

(a) MV collector system (b) Eq. Cable pi model

FIGURE 4. Aggregated single-machine model of MV collector system.

Figure 5 shows the typical configuration of an OWF with radially distributed MV collector systems. Each MV main bus connects M arrays of WTs, and in the m array, N_m WTs are interconnected through N_m sections of collecting cables.

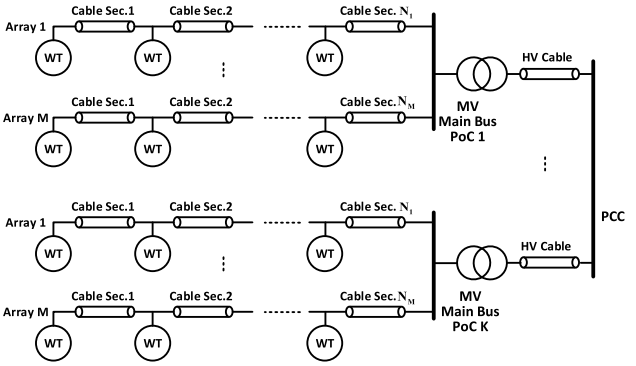

FIGURE 5. Typical radially distributed OWF configuration.

A. POWER LOSS BASED AGGREGATION MODEL

Assuming each WT injects the same amount of current $\underline{I}_{\mathrm{WT}}$ at fundamental frequency, the total current contributed from the radial m is given by

$$\underline{I}_m = \sum_{n=1}^{N_m} \underline{I}_{m,n} = N_m \underline{I}_{\mathrm{WT}}, \;\; m = 1, 2, \ldots, M, \;\; n = 1, 2, \ldots, N \tag{29}$$

where n represents the n^{th} WT in the array m and $\underline{I}_{m,n}$ denotes the injected current. For each cable section, the nominal PI model with lumped parameters is adopted [29]. If defining the equivalent series impedance of all the cable sections in the array m as $\underline{Z}_m$, the power loss in the array m can be represented by

$$\underline{I}_m^2 \underline{Z}_m = \sum_{n=1}^{N_m} \left(n \frac{\underline{I}_{m,n}}{N_m} \right)^2 \underline{Z}_{m,n} \tag{30}$$

where $\underline{Z}_{m,n} = R_{m,n} + sL_{m,n}$ denotes the series impedance of the cable section which connects the n^{th} WT and the $(n+1)^{\mathrm{th}}$

WT in the array m. Combining (29) and (30), $\underline{Z}_m$ is solved as

$$\underline{Z}_m = \frac{1}{N_m^2}\sum_{n=1}^{N_m} n^2 \underline{Z}_{m,n} \tag{31}$$

Combining the current and power loss equations as given in (32), the equivalent series impedance $\underline{Z}_{\mathrm{mvc}}$ of all the cables of a MV collector system as well as the lumped resistance R_{mvc} and inductance L_{mvc} can be solved, as shown in (33).

$$\begin{aligned}
\underline{I}_{\mathrm{mv}} &= \sum_{m=1}^{M} \underline{I}_m = \sum_{m=1}^{M} N_m \underline{I}_{\mathrm{WT}}, \quad m = 1, 2, \ldots, M \\
\underline{I}_{\mathrm{mv}}^2 \underline{Z}_{\mathrm{mvc}} &= \sum_{m=1}^{M} \underline{I}_m^2 \underline{Z}_m \qquad (32) \\
\underline{Z}_{\mathrm{mvc}} &= \sum_{m=1}^{M} \underline{I}_m^2 \underline{Z}_m \Big/ \underline{I}_{\mathrm{mv}}^2 = \sum_{m=1}^{M} N_m^2 \underline{Z}_m \Big/ \left(\sum_{m=1}^{M} N_m\right)^2 \\
\underline{Z}_{\mathrm{mvc}}(\omega_1) &= R_{\mathrm{mvc}} + \mathrm{j}\omega_1 L_{\mathrm{mvc}} \qquad (33)
\end{aligned}$$

For the aggregation of the shunt admittance of the distributed cables, the capacitances of all the cable sections can be simply added together [26]. So the equivalent capacitance C_{mv} and the resulted shunt admittance $\underline{Y}_{\mathrm{mv}}$ of a MV collector system can be represented by

$$C_{\mathrm{mvc}} = \sum_{m=1}^{M}\sum_{n=1}^{N} C_{m,n}, \ \underline{Y}_{\mathrm{mvc}} = \mathrm{j}\omega C_{\mathrm{mvc}} \tag{34}$$

As for the aggregation of WTs, all the WTs of a MV collector system can be assumed in direct parallel connection due to negligible series impedances of the collecting cables compared with WT impedances. Furtherly assuming all the WTs are under the same operating point, the equivalent impedance of the WTs taking into account the terminal filters and step-up transformers can be represented by

$$\underline{\boldsymbol{Z}}_{\mathrm{wt,agg}} = \left((\underline{\boldsymbol{Z}}_{\mathrm{wt}}^{-1} + 1/\underline{Z}_{\mathrm{F}}\boldsymbol{E})^{-1} + \underline{Z}_{\mathrm{T}}\boldsymbol{E}\right)/N_{\mathrm{wt}} \tag{35}$$

where $\underline{\boldsymbol{Z}}_{\mathrm{wt}}$ is the abbreviation for $\underline{\boldsymbol{Z}}_{\mathrm{wt,pn}}$, $\underline{Z}_{\mathrm{F}}$ represents the impedance of WT terminal filter, $\underline{Z}_{\mathrm{T}}$ represents the impedance of WT step-up transformer and N_{wt} is the total number of WTs.

Finally, the output impedance of the aggregated MV collector system as illustrated in Figure 4 can be written as

$$\underline{\boldsymbol{Z}}_{\mathrm{mv}} = \left(\left((\underline{\boldsymbol{Z}}_{\mathrm{wt,agg}}^{-1} + 0.5\underline{Y}_{\mathrm{mvc}}\boldsymbol{E})^{-1} + \underline{Z}_{\mathrm{mvc}}\boldsymbol{E}\right)^{-1} + 0.5\underline{Y}_{\mathrm{mvc}}\boldsymbol{E}\right)^{-1} \tag{36}$$

B. VOLTAGE DROP BASED AGGREGATION MODEL

For the same MV collector system as shown in Figure 5, the voltage drop of the m^{th} wind array can be represented by

$$\underline{I}_m \underline{Z}_m = \sum_{n=1}^{N_m} n\underline{I}_{m,n}\underline{Z}_{m,n} = \sum_{n=1}^{N_m} n\frac{\underline{I}_m}{N_m}\underline{Z}_{m,n} \tag{37}$$

where $\underline{Z}_m$ denotes the equivalent impedance of that array. According to the current relationship as given in (29), $\underline{Z}_m$ can be solved as

$$\underline{Z}_m = \frac{1}{N_m}\sum_{n=1}^{N_m} n\underline{Z}_{m,n} \tag{38}$$

Furtherly according to the parallel circuit theory, the equivalent series impedance of all the cables of a MV collector system can be represented by

$$\underline{Z}_{\mathrm{mvc}} = \frac{1}{\sum_{m=1}^{M} 1/\underline{Z}_m} \tag{39}$$

For the aggregation of the shunt admittance of the distributed cables, the equations in (34) still apply. The equivalent impedance of all the WTs can be derived as in (35) and the equivalent output impedance of the MV collector system can be deduced as in (36).

C. DETAILED MODEL AND ACCURACY ANALYSIS

Figure 6 shows the equivalent circuit of the m^{th} wind array of a MV collector system. Neglecting the voltage differences among WT terminals, all WTs can be modelled with the same output impedance, thus the output admittance of the wind array can be derived as in (40). The output impedance of the wind array $\underline{\boldsymbol{Z}}_{\mathrm{m,str}}$ as well as the output impedance of the complete MV collector system $\underline{\boldsymbol{Z}}_{\mathrm{mv}}$ can be derived as in (41).

$$\begin{aligned}
\underline{\boldsymbol{Y}}_{1,\mathrm{sec}} &= \left(\underline{Z}_{m,1}\boldsymbol{E} + \left(0.5\underline{Y}_{m,1}\boldsymbol{E} + \underline{\boldsymbol{Z}}_{\mathrm{wt}}^{-1}\right)^{-1}\right)^{-1} + 0.5\underline{Y}_{m,1}\boldsymbol{E} \\
\underline{\boldsymbol{Y}}_{2,\mathrm{secs}} &= \left(\underline{Z}_{m,2}\boldsymbol{E} + \left(0.5\underline{Y}_{m,2}\boldsymbol{E} + \underline{\boldsymbol{Z}}_{\mathrm{wt}}^{-1} + \underline{\boldsymbol{Y}}_{1\,\mathrm{sec}}\right)^{-1}\right)^{-1} \\
&\quad + 0.5\underline{Y}_{m,2}\boldsymbol{E} \qquad (40) \\
&\cdots \\
\underline{\boldsymbol{Y}}_{N,\mathrm{secs}} &= \Big(\underline{Z}_{m,N}\boldsymbol{E} + \Big(0.5\underline{Y}_{m,N}\boldsymbol{E} + \underline{\boldsymbol{Z}}_{\mathrm{wt}}^{-1} \\
&\quad + \underline{\boldsymbol{Y}}_{N-1,\mathrm{sec}\,s}\Big)^{-1}\Big)^{-1} + 0.5\underline{Y}_{m,N}\boldsymbol{E} \\
\underline{\boldsymbol{Z}}_{m,\mathrm{str}} &= \underline{\boldsymbol{Y}}_{N,\mathrm{sec\,s}}^{-1} \\
\underline{\boldsymbol{Z}}_{\mathrm{mv}} &= \left(\sum_{m=1}^{M} \underline{\boldsymbol{Z}}_{m,\mathrm{str}}^{-1}\right)^{-1} \qquad (41)
\end{aligned}$$

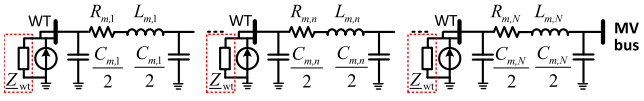

FIGURE 6. Equivalent circuit of the m^{th} wind array.

The detailed model derived in (40) and (41) is then used to check the accuracies of the aggregated single-machine models. The test MV collector system is set to have 40 WTs distributed in 6 wind arrays. The cable settings of the MV collector system are shown in Figure 7, in which the parameters of the cable sections are estimated from ABB user's guide for submarine systems [30], as presented in Appendix B. The frequency scanning of the aggregated models and the

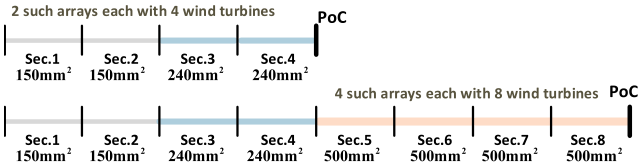

FIGURE 7. Cable settings of the test MV collector system.

detailed impedance model is shown in Figure 8. For the detailed impedance model, an extra scenario without considering cable capacitances is shown for comparison. For space reason, only the positive sequence impedance $\underline{Z}_{\mathrm{pp}}$ and the coupling term $\underline{Z}_{\mathrm{pn}}$ are presented. Same observations can be seen for the other impedance terms. For this specific MV collector system, neglecting the cable capacitances introduces large error at the frequencies starting from 200 Hz, while the power loss and voltage drop based aggregation models show acceptable accuracy at the frequencies between 5 Hz and 3 kHz.

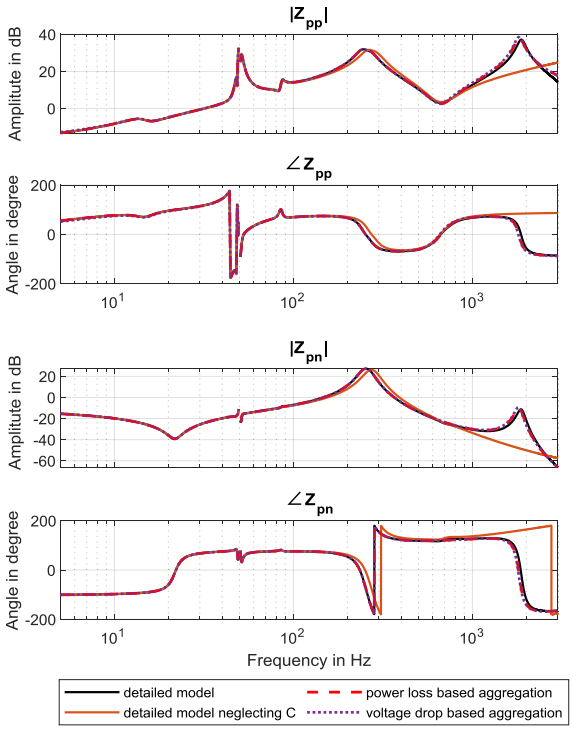

FIGURE 8. Frequency scanning to different impedance models of the test MV collector system.

IV. RESONANCE ANALYSIS OF DFIG-BASED OWF WITH HVDC CONNECTION

Figure 9 shows the test grid and relevant parameters. A 400 MW OWF with 80 DFIG-based WTs are connected to an offshore HVDC converter station through short high voltage submarine cables. The MV collector systems are represented by the power loss based aggregation model as derived in Section III.

The HVDC link is assumed to have a constant DC voltage due to its strong onshore grid connection. The wind farm side VSC converter (WFVSC) is regulated to maintain a constant AC voltage for the connected OWF. For the purpose of better dynamic performance, a single loop PI control structure is adopted in the WFVSC [31], [32]. Since there is no PLL and the dq frame control is symmetrical, the AC side sequence impedances of the WFVSC are frequency-decoupled, which can be written as

$$\begin{aligned}\underline{Z}_{\mathrm{vsc,p}}(s) &= \frac{R_{\mathrm{c}}+sL_{\mathrm{c}}-\mathrm{j}K_{\mathrm{d}}K_{\mathrm{pwm}}\underline{G}_{\mathrm{d}}(s-\mathrm{j}\omega_1)}{1+K_{\mathrm{pwm}}\underline{H}_{\mathrm{PI}}(s-\mathrm{j}\omega_1)\,\underline{G}_{\mathrm{d}}(s-\mathrm{j}\omega_1)}\\ \underline{Z}_{\mathrm{vsc,n}}(s) &= \frac{R_{\mathrm{c}}+sL_{\mathrm{c}}+\mathrm{j}K_{\mathrm{d}}K_{\mathrm{pwm}}\underline{G}_{\mathrm{d}}(s+\mathrm{j}\omega_1)}{1+K_{\mathrm{pwm}}\underline{H}_{\mathrm{PI}}(s+\mathrm{j}\omega_1)\,\underline{G}_{\mathrm{d}}(s+\mathrm{j}\omega_1)}\end{aligned} \tag{42}$$

where $\underline{Z}_{\mathrm{vsc,p}}(s)$ denotes the positive sequence impedance, $\underline{Z}_{\mathrm{vsc,n}}(s)$ denotes the negative sequence impedance, $\underline{G}_{\mathrm{d}}(s) = 1/(1+1.5T_{\mathrm{s}}s)$, $\underline{H}_{\mathrm{PI}}(s) = K_{\mathrm{vp}} + K_{\mathrm{vi}}/s$ and K_{pwm} is the gain of the PWM unit. Taking into account the AC filters and the coupling transformer of the WFVSC, the positive- and negative-sequence impedances of the HVDC grid connection can be derived as

$$\begin{aligned}\underline{Z}_{\mathrm{G,p}}(s) &= 1/(1/\underline{Z}_{\mathrm{vsc,p}}(s)+1/\underline{Z}_{\mathrm{filters}}(s))+\underline{Z}_{\mathrm{ctr}}(s)\\ \underline{Z}_{\mathrm{G,n}}(s) &= 1/(1/\underline{Z}_{\mathrm{vsc,n}}(s)+1/\underline{Z}_{\mathrm{filters}}(s))+\underline{Z}_{\mathrm{ctr}}(s)\end{aligned} \tag{43}$$

where $\underline{Z}_{\mathrm{filters}}(s)$ denotes the overall impedance of the 5$^{\mathrm{th}}$ and 7$^{\mathrm{th}}$ single-tuned filters as well as the 27$^{\mathrm{th}}$ and 54$^{\mathrm{th}}$ high-pass damped filters, and $\underline{Z}_{\mathrm{ctr}}(s)$ denotes the short circuit impedance of the coupling transformer.

Since the two 155 kV branches of the OWF are identical, the equivalent output impedance of the OWF looking from PCC can be formulated as

$$\underline{\mathbf{Z}}_{\mathrm{WF,pn}}(s) = \frac{1}{2}\left(\left((\underline{\mathbf{Z}}_{\mathrm{mv}}^{-1}+\underline{\mathbf{Z}}_{\mathrm{T}}+0.5\underline{\boldsymbol{Y}}_{\mathrm{hvc}})^{-1}+\underline{\mathbf{Z}}_{\mathrm{hvc}}\right)^{-1} + 0.5\underline{\boldsymbol{Y}}_{\mathrm{hvc}}\right)^{-1} \tag{44}$$

where

$$\underline{\mathbf{Z}}_{\mathrm{T}} = \begin{bmatrix}\underline{Z}_{\mathrm{T}} & 0\\ 0 & \underline{Z}_{\mathrm{T}}\end{bmatrix}\underline{\mathbf{Z}}_{\mathrm{hvc}} = \begin{bmatrix}\underline{Z}_{\mathrm{hvc}} & 0\\ 0 & \underline{Z}_{\mathrm{hvc}}\end{bmatrix}\underline{\boldsymbol{Y}}_{\mathrm{hvc}} = \begin{bmatrix}\underline{Y}_{\mathrm{hvc}} & 0\\ 0 & \underline{Y}_{\mathrm{hvc}}\end{bmatrix}$$

with $\underline{Z}_{\mathrm{T}}$ denoting the short circuit impedance of the 33 / 155 kV wind farm transformer, $\underline{Z}_{\mathrm{hvc}}$ and $\underline{Y}_{\mathrm{hvc}}$ denoting the series impedance and shunt admittance of the 155 kV cables. The nonzero off-diagonal elements of the sequence impedance matrix $\underline{\mathbf{Z}}_{\mathrm{WF,pn}}(s)$ as defined in

$$\underline{\mathbf{Z}}_{\mathrm{WF,pn}}(s) = \begin{bmatrix}\underline{Z}_{\mathrm{WF,pp}}(s) & \underline{Z}_{\mathrm{WF,pn}}(s)\\ \underline{Z}_{\mathrm{WF,np}}(s) & \underline{Z}_{\mathrm{WF,nn}}(s)\end{bmatrix} \tag{45}$$

make the DFIG-based OWF with HVDC grid connection a MIMO system. The root causes of the coupling between the positive and negative sequence impedances of the OWF are the PLL and asymmetrical d- and q-axis control structures in the DFIG energy conversion systems. For the better understanding of the impedance coupling in (45), the sequence equivalents of the investigated MIMO system in case of a shunt current perturbation are presented in Figure 10.

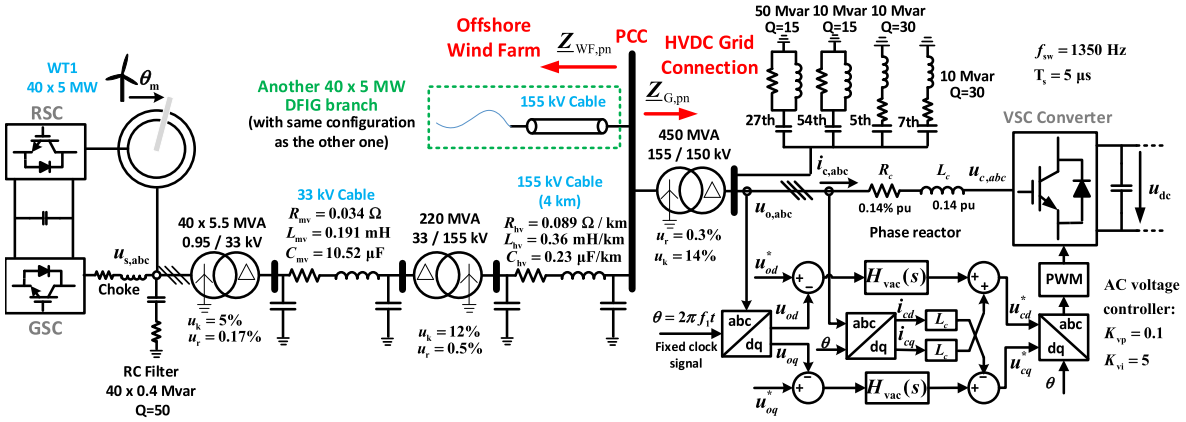

FIGURE 9. Diagram of an aggregated DFIG-based OWF with a two-level VSC-based HVDC connection.

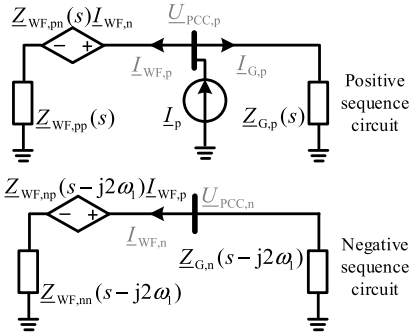

FIGURE 10. Sequence equivalents of the HVDC-connected OWF. The perturbation $\underline{I}_{\mathrm{p}}$ and the responses $\underline{U}_{\mathrm{PCC,p}}, \underline{I}_{\mathrm{WF,p}}, \underline{I}_{\mathrm{G,p}}$ are at frequency ω_{p} and the responses $\underline{U}_{\mathrm{PCC,n}}, \underline{I}_{\mathrm{WF,n}}$ are at the frequency $\omega_{\mathrm{p}} - 2\omega_1$.

Given a positive sequence current perturbation $\underline{I}_{\mathrm{p}}$ at the frequency ω_{p}, the system will have both the positive sequence responses $\underline{U}_{\mathrm{PCC,p}}$, $\underline{I}_{\mathrm{WF,p}}, \underline{I}_{\mathrm{G,p}}$ at the same frequency and the negative sequence responses $\underline{U}_{\mathrm{PCC,n}}, \underline{I}_{\mathrm{WF,n}}$ at the frequency $\omega_{\mathrm{p}} - 2\omega_1$. Note that for $\omega_{\mathrm{p}} < 2\omega_1$, the negative sequence responses at the frequency $\omega_{\mathrm{p}} - 2\omega_1$ actually correspond to the positive sequence responses $\underline{U}^*_{\mathrm{PCC,n}}$, $\underline{I}^*_{\mathrm{WF,n}}$ at the frequency $2\omega_1 - \omega_{\mathrm{p}}$ [34], where the superscript * denotes the conjugation operation.

In terms of the positive sequence current perturbation, the sequence equivalents of the HVDC-connected OWF as given in Figure 10 can be formulated as

$$\begin{aligned}
\underline{U}_{\mathrm{PCC,p}} &= \underline{Z}_{\mathrm{WF,pp}}(s)\underline{I}_{\mathrm{WF,p}} + \underline{Z}_{\mathrm{WF,pn}}(s)\underline{I}_{\mathrm{WF,n}} \\
\underline{U}_{\mathrm{PCC,p}} &= \underline{I}_{\mathrm{G,p}}\underline{Z}_{\mathrm{G,p}}(s) \\
\underline{U}_{\mathrm{PCC,n}} &= \underline{Z}_{\mathrm{WF,nn}}(s - \mathrm{j}2\omega_1)\underline{I}_{\mathrm{WF,n}} + \underline{Z}_{\mathrm{WF,np}}(s - \mathrm{j}2\omega_1)\underline{I}_{\mathrm{WF,p}} \\
\underline{U}_{\mathrm{PCC,n}} &= -\underline{I}_{\mathrm{WF,n}}\underline{Z}_{\mathrm{G,p}}(s - \mathrm{j}2\omega_1)
\end{aligned} \tag{46}$$

Jointly solving the equations in (46) yields the equivalent SISO sequence impedances of the wind farm, as given in

$$\begin{aligned}
&\underline{Z}_{\mathrm{WF,p}}(s) \\
&\quad = \underline{U}_{\mathrm{PCC,p}}/\underline{I}_{\mathrm{WF,p}} \\
&\quad = \underline{Z}_{\mathrm{WF,pp}}(s) - \frac{\underline{Z}_{\mathrm{WF,pn}}(s)\underline{Z}_{\mathrm{WF,np}}(s - \mathrm{j}2\omega_1)}{\underline{Z}_{\mathrm{WF,nn}}(s - \mathrm{j}2\omega_1) + \underline{Z}_{\mathrm{G,n}}(s - \mathrm{j}2\omega_1)}
\end{aligned}$$

$$\begin{aligned}
&\underline{Z}_{\mathrm{WF,n}}(s - \mathrm{j}2\omega_1) \\
&\quad = \underline{U}_{\mathrm{PCC,n}}/\underline{I}_{\mathrm{WF,n}} \\
&\quad = \underline{Z}_{\mathrm{WF,nn}}(s - \mathrm{j}2\omega_1) - \frac{\underline{Z}_{\mathrm{WF,pn}}(s)\underline{Z}_{\mathrm{WF,np}}(s - \mathrm{j}2\omega_1)}{\underline{Z}_{\mathrm{WF,pp}}(s) + \underline{Z}_{\mathrm{G,p}}(s)}
\end{aligned} \tag{47}$$

where $\underline{Z}_{\mathrm{WF,p}}(s)$ denotes the equivalent SISO positive sequence impedance, $\underline{Z}_{\mathrm{WF,n}}(s - \mathrm{j}2\omega_1)$ denotes the equivalent SISO negative sequence impedance with the frequency shifting of $2\omega_1$, and the last term in each impedance equation interprets the frequency coupling. The frequency couplings as represented in (47) are not only determined by the off-diagonal elements of the wind farm impedance $\underline{\boldsymbol{Z}}_{\mathrm{WF,pn}}(s)$, but also determined by the diagonal elements of $\underline{\boldsymbol{Z}}_{\mathrm{WF,pn}}(s)$ as well as the grid impedances $\underline{Z}_{\mathrm{G,p}}(s)$ and $\underline{Z}_{\mathrm{G,n}}(s)$ that are related to all the grid components of the system. The strength of frequency couplings can be evaluated by the proximity of the real sequence impedances to the equivalent SISO sequence impedances, i.e. the proximity of $\underline{Z}_{\mathrm{WF,pp}}(s)$ to $\underline{Z}_{\mathrm{WF,p}}(s)$ and the proximity of $\underline{Z}_{\mathrm{WF,nn}}(s)$ to $\underline{Z}_{\mathrm{WF,n}}(s)$.

For the identification of the resonances in the frequency-coupled MIMO system, the PCC nodal impedances of the equivalent SISO sequence systems as formulated in (48) will be used. Through performing frequency scanning to $\underline{Z}_{\mathrm{PCC,p}}(s)$ and $\underline{Z}_{\mathrm{PCC,n}}(s)$, the resonances of the system can be found by the peaks of the magnitude versus frequency plots, and the damping of the resonances can be determined by the angle variations around the resonance frequencies in the angle versus frequency plots. If the phase variation around a resonance frequency is greater than 180°, i.e. a resonance with negative damping, the resonance is unstable [2]. Otherwise, the resonance may amplify the harmonic distortion at the resonance frequency and the amplification degree is proportional to the impedance magnitude.

$$\begin{aligned}
\underline{Z}_{\mathrm{PCC,p}}(s) &= \frac{\underline{Z}_{\mathrm{WF,p}}(s)\underline{Z}_{\mathrm{G,p}}(s)}{\underline{Z}_{\mathrm{WF,p}}(s) + \underline{Z}_{\mathrm{G,p}}(s)} \\
\underline{Z}_{\mathrm{PCC,n}}(s) &= \frac{\underline{Z}_{\mathrm{WF,n}}(s)\underline{Z}_{\mathrm{G,n}}(s)}{\underline{Z}_{\mathrm{WF,n}}(s) + \underline{Z}_{\mathrm{G,n}}(s)}
\end{aligned} \tag{48}$$

In the authors' previous work [2], it is demonstrated when DFIG-based OWF operates under low wind speed or receives a control command for lowering its active power output, the rotor speed of the wind turbines will be decreased and it can increase the risk of SSR instability. Additionally, the variation of the in-service WTs as well as the change of the switching states of the MV collector cables can greatly change the resonance frequencies and increase the risk of resonance stimulation under critical conditions. On this basis, this paper will no longer comprehensively analyze the risk of resonances with respect to various operating conditions and grid configurations, but show the impact of frequency coupling on the risk of resonances using two simple cases: (1) control parameter variation; (2) grid topology change.

A. IN CASE OF CONTROL PARAMETER VARIATION

A lot of publications have shown the negative influence of a large proportional coefficient of the RSC current controller $\underline{H}_{\mathrm{ri}}(s) = K_{\mathrm{rp}} + K_{\mathrm{ri}}/s$ on SSR stability [7], [8], [33]. Figure 11 shows the impedance responses of the simulated DFIG system under different K_{rp}. It is observed, as K_{rp} increases, the angles of the positive sequence impedance $\underline{Z}_{\mathrm{pp}}$ and the coupling impedances $\underline{Z}_{\mathrm{pn}}$ and $\underline{Z}_{\mathrm{np}}$ will increase to be above 90° or decrease to be below −90° in the subsynchronous frequency area, which indicates negative resistances at the corresponding frequencies. For the scenarios $K_{\mathrm{rp}} = 0.15$ and $K_{\mathrm{rp}} = 0.45$, the impact of K_{rp} on the frequency coupling of the investigated DFIG-based OWF is shown in Figure 12. To reflect the resonance points of the studied MIMO system, the positive sequence impedance of the connected HVDC system is also shown in Figure 12. Through comparing $\underline{Z}_{\mathrm{WF,p}}$ with $\underline{Z}_{\mathrm{WF,pp}}$, it can be observed the frequency coupling mainly exists in the frequency range less than 100 Hz, and the strength or the degree of the frequency coupling in the scenario $K_{\mathrm{rp}} = 0.45$ is greater than that in the scenario $K_{\mathrm{rp}} = 0.15$. At the frequencies above 100 Hz, the frequency coupling is not observable, thus can be neglected. Since the impact of the frequency coupling on the negative sequence impedance of the investigated OWF is negligible, it is not shown here.

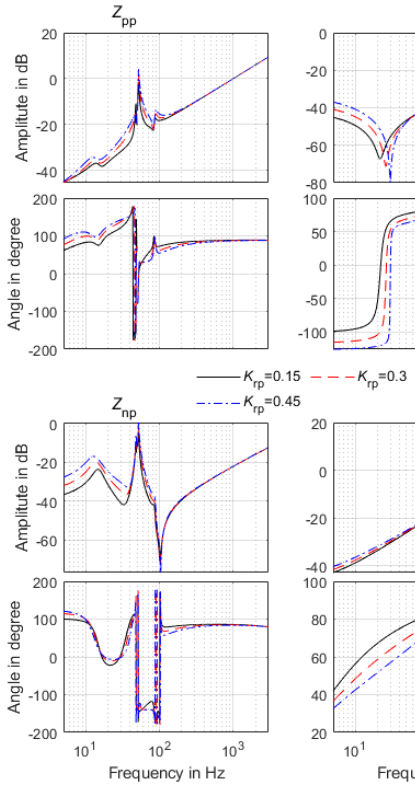

FIGURE 11. Impact of the proportional coefficient K_{rp} of the RSC current controller on the output impedances of the simulated DFIG-based WT.

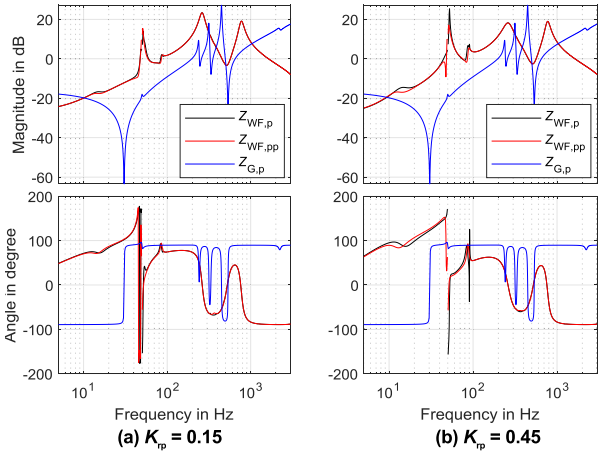

FIGURE 12. The real and equivalent SISO positive sequence impedances of the investigated OWF as well as the positive sequence impedance of the HVDC grid connection.

In Figure 12, it can also be observed, there are several resonance points determined by the cross-points of the magnitudes of $\underline{Z}_{\mathrm{WF,p}}/\underline{Z}_{\mathrm{WF,pp}}$ and $\underline{Z}_{\mathrm{G,p}}$ and the variation of K_{rp} mainly influences the SSR resonance mode. To better show the impact of the frequency coupling on the SSR, the PCC nodal impedances of the equivalent SISO positive sequence system as well as the corresponding impedances neglecting the frequency coupling are shown in Figure 13. In Figure 13 (a), the frequency coupling is included. For the scenarios $K_{\mathrm{rp}} = 0.45$ and $K_{\mathrm{rp}} = 0.5$, the resonance peaks at around 10 Hz and 90 Hz in the magnitude plots indicate strong frequency coupling and the negative real part values of the PCC nodal impedances at the SSR frequencies indicate SSR instability [2]. As for the PCC nodal impedances neglecting the frequency coupling (by setting $\underline{Z}_{\mathrm{WF,p}} = \underline{Z}_{\mathrm{WF,pp}}$), the SSR mode is stable for $K_{\mathrm{rp}} = 0.45$, which is indicated by the positive real part value of the impedance at the SSR frequency, as shown in Figure 13 (b). Thus for the scenario $K_{\mathrm{rp}} = 0.45$, neglecting the frequency coupling leads to a wrong stability assessment result.

In practical operating conditions, the HVDC connected DFIG-based OWF may also have such SSR instability risks when wind speed is quite low or the OWF receives a lowering power generation command from its superior level control

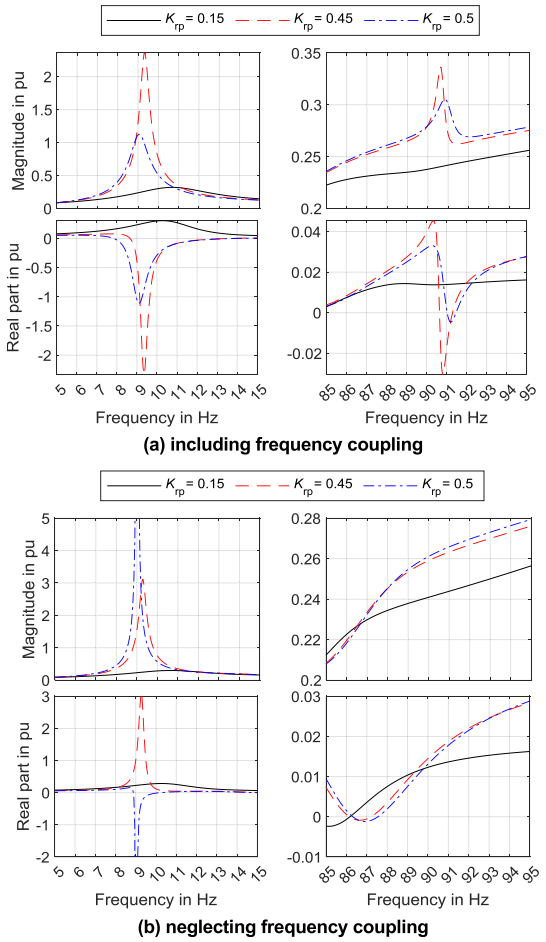

FIGURE 13. Impact of K_{rp} on the PCC nodal impedances of the equivalent SISO positive sequence system at frequencies below 100 Hz.

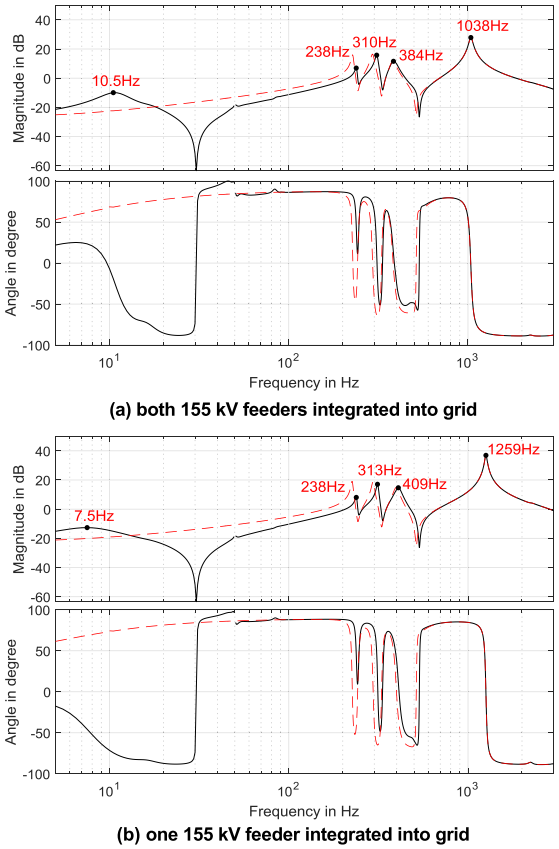

FIGURE 14. Impact of the grid topology change on the PCC nodal impedances. Solid lines: equivalent SISO positive sequence system. Dashed lines: equivalent SISO negative sequence system.

center [2], [7]. Therefore, including frequency coupling in the modelling and resonance analysis plays an important role in the correct identification of low-frequency resonance stability and can help system operators to take proper preventive corrections.

B. IN CASE OF GRID TOPOLOGY CHANGE

By the startup or shutdown of the investigated OWF or when a three-phase fault occurs to one of the two HV feeders in the OWF, the system may go through the transition from both 155 kV branches integrated into grid (with 400 MW feed-in power) to only one 155 kV branch integrated into grid (with 200 MW feed-in power). The dominating resonance modes of the system can be more or less varied, as shown in Figure 14.

As observed, following the change of the grid topology, the last resonance mode is most significantly influenced. The resonance frequency is varied from 1038 Hz to 1259 Hz, which matches the sideband frequency of the wind farm side HVDC converter, moreover, the impedance magnitute of this resonance mode is largely increased. The stimulation of the resonance can greatly amplify the switching harmonics and limit the power transfer along the MV and HV cables. For the other resonance modes, the influence of the grid topology change on them are relatively small. Since the frequency coupling mainly exists in the low-frequency area and the SSR mode maintains sufficient phase margin following the grid topology change, ignorging the frequency coupling effect will not have much influence on the SSR stablity as well as on the risks of the other resonance modes.

When taking into account various operating conditions and grid configurations, the resonance frequencies of the dominating resonance modes in Figure 14 can be changed by up to 1 kHz and sharp resonance peaks can be introduced [2]. The existance of the charateristic harmonics may cause the stimulation of one or more resonances and induce the amplification of harmonic distortions. Generally, as long as the resonances do not make the system enter into critical stable states, the frequency coupling effect can be neglected for the simplicity of resonance analysis.

V. SIMULATION VALIDATION

To validate the results of the theoretical modelling and resonance analysis as presented in Chapters II-IV, the detailed DFIG model developed by MATLAB is adopted in simulation [24]. Note that the control structure of the wind turbine is modified according to Figure 1. The test grid as shown in Figure 9 is built in MATLAB / Simulink. The parameters

of the MV collector systems (including cables and WTs) and the aggregated single-machine representations are available in Appendix B and C. The DC side of the offshore HVDC converter station is simplified to an ideal DC voltage source.

A. MODEL VERIFICATION

To measure the impedance responses of the simulated DFIG-based WT, the MV collector system, as well as the two-level VSC based HVDC converter under small-signal perturbations, the series voltage injection approach as discussed in [23], [35] is applied in simulations.

In each simulation, the measured object is connected to an infinite bus or a resistive load. To handle the enormous computation burden of tens of DFIG-based WTs in MATLAB/Simulink, the model validation of the aggregated MV collector system is divided into 2 steps. In the first step simulations, the impedance reponses of an 8-WT array and a 4-WT array are measured respectively, in which each WT is represented by the detailed DFIG model and each cable subsection is represented by the distributed parameters cable model from Simulink library. In the second step simulations, the impedance reponses of the MV collector system with each wind array represented by a single-machine model are measured. Figure 15, 16 and 17 shows the good match of the analytical models with the simulation results.

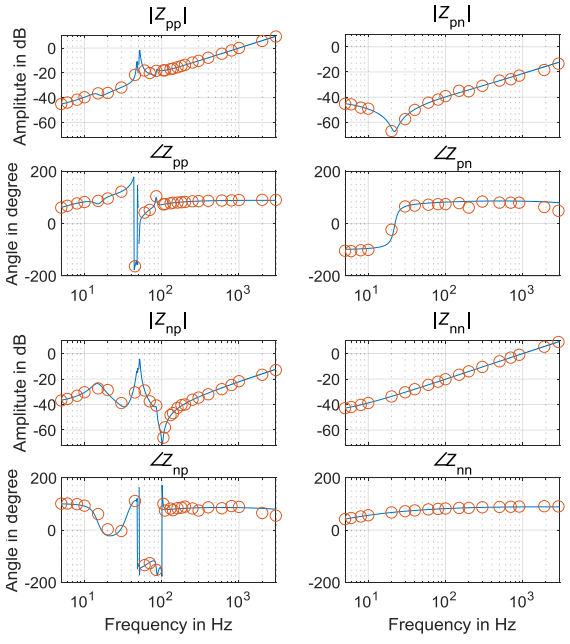

FIGURE 15. Comparison of the analytical model with the simulation impedance responses of the studied DFIG-based WT. Solid lines: analytical models; Circles: numerical simulation results.

B. RESONANCE STIMULATION AND STABILITY ASSESSMENT

Figure 18 shows the simulation results in case of control parameter variation, when K_{rp} is varied from 0.15 to 0.45 at 10 s, the system becomes unstable due to the formation of

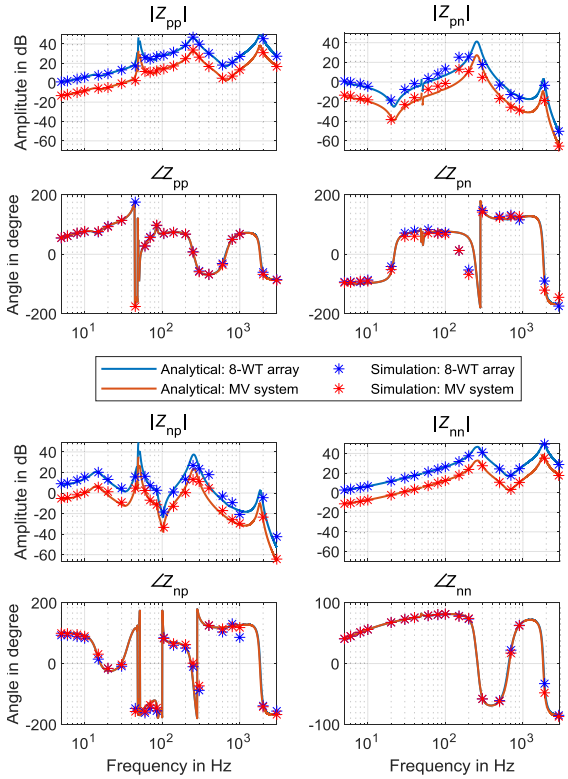

FIGURE 16. Comparison of the analytical aggregation models with the simulation impedance responses of an 8-WT array and the MV collector system.

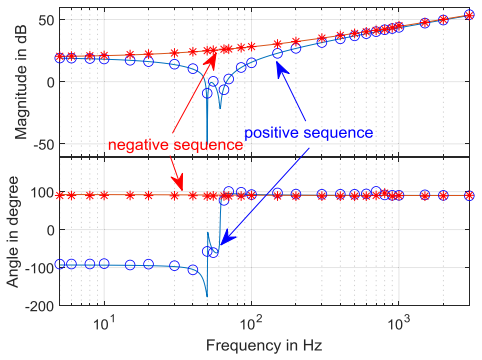

FIGURE 17. Comparison of the analytical model with the simulation impedance responses of the wind farm side HVDC converter. Solid lines: analytical models; Asterisks and circles: numerical simulation results.

the strong PCC current oscillation, which verifies the theoretical analysis on the SSR stability assessment as presented in Section IV. A. The frequency and damping of the SSR actually vary continuously with the growth of the resonance due to the strong nonlinearities in the converter control induced by the large SSR current [7], [36].

Figure 19 shows the simulations results in case of grid topology change. When an HV feeder of the OWF is disconnected from the grid at 10 s, large high-frequency ripples are observed in the PCC voltage waveform. According to the FFT analysis as shown in Figure 20, they are induced by the resonance amplification of the sideband harmonics

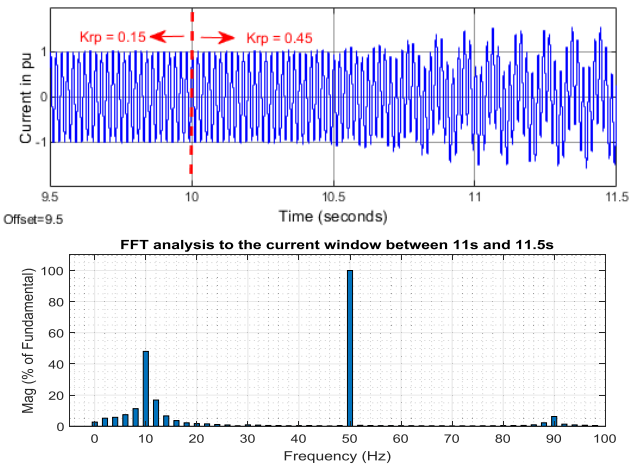

FIGURE 18. PCC current and FFT analysis as K_{rp} varies.

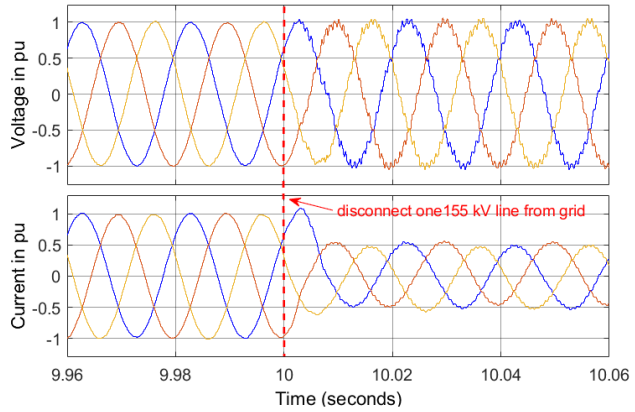

FIGURE 19. PCC voltage and current following the grid topology change.

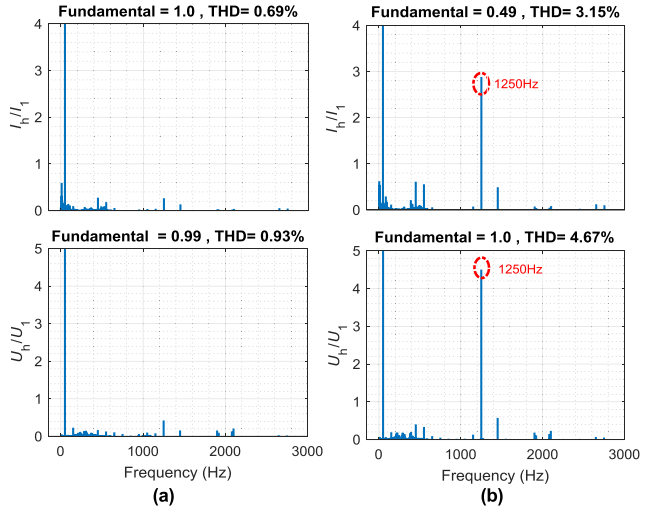

FIGURE 20. PCC current and voltage FFT analysis. (a) Both 155 kV feeders integrated into grid; (b) one 155 kV feeder disconnected from grid.

of the HVDC converter, which verifies the results of the theoretical analysis as presented in Section IV.B. According to the recommended harmonic distortion limits as given in [1], the 1250 Hz voltage harmonic in Figure 20 (b) violates the limit of 1.5% times of the fundamental value, and the total harmonic distortion (THD) of the PCC voltage in Figure 20 (b) violates the limit of 2.5% times of the fundamental value.

VI. CONCLUSION

This paper presented the comprehensive impedance modelling of DFIG-based wind turbine considering all the relevant control dynamics for the frequency range from several Hz to a few kHz. Through stepwise simulation verifications, the equivalent power loss based aggregation model of a large-scale DFIG-based OWF was validated to be feasible for wide frequency range of resonance analysis.

The resonances in the DFIG-based OWF with HVDC connection were investigated using the PCC nodal impedances of the equivalent SISO sequence systems. The impact of the frequency coupling effect on the risks of resonances was analyzed. Harmonic amplification and SSR stability issues were demonstrated taking into account grid topology change and control parameter variation.

The discussed frequency coupling of fundamental frequency was found crucial when a SSR resonance mode is approaching critically-damped stable state. When a SSR resonance mode maintains sufficient damping regarding possible operating conditions and grid configurations, the frequency coupling effect can be neglected in the wideband resonance analysis for simplicity.

For further works, the detailed modelling of pulse width modulation (PWM) should also be integrated in resonance analysis to address the extra frequency coupling of PWM switching frequency, especially when the investigated frequency range involves above half of the switching frequency.

APPENDIX

A. SYMBOLS DEFINITION

Detailed expressions of $\underline{\boldsymbol{Y}}_{\mathrm{gsc}}$ and $\underline{\boldsymbol{a}}_{2\times1}$ in (9) can be written as

$$\begin{aligned}\underline{\boldsymbol{Y}}_{\mathrm{gsc}} &= \left[\underline{\boldsymbol{Z}}_{\mathrm{RL}} + \left(\underline{\boldsymbol{G}}_{\mathrm{gi}} + \boldsymbol{K}_{\mathrm{gd}}\right)\underline{G}_{\mathrm{d}}U_{\mathrm{dc0}}\right]^{-1} \\ &\quad \cdot \left\{\boldsymbol{E} - \left[\underline{\boldsymbol{G}}^{\mathrm{m}}_{\mathrm{PLL}} + \underline{\boldsymbol{G}}^{\mathrm{u}}_{\mathrm{PLL}}\right. \right. \\ &\quad \left. \left. + \left(\underline{\boldsymbol{G}}_{\mathrm{gi}} + \boldsymbol{K}_{\mathrm{gd}}\right)\underline{\boldsymbol{G}}^{\mathrm{i}}_{\mathrm{PLL}}\right]\underline{G}_{\mathrm{d}}U_{\mathrm{dc0}}\right\} \\ \underline{\boldsymbol{a}}_{2\times1} &= \left[\underline{\boldsymbol{Z}}_{\mathrm{RL}} + \left(\underline{\boldsymbol{G}}_{\mathrm{gi}} + \boldsymbol{K}_{\mathrm{gd}}\right)\underline{G}_{\mathrm{d}}U_{\mathrm{dc0}}\right]^{-1} \\ &\quad \times \left(\underline{\boldsymbol{G}}_{\mathrm{gi}}\underline{\boldsymbol{h}}_{\mathrm{vdc}}\underline{G}_{\mathrm{d}}U_{\mathrm{dc0}} + \boldsymbol{M}_{\mathrm{g1}}\underline{G}_{\mathrm{d}}\right)\end{aligned} \tag{A1}$$

Detailed expressions of $\underline{\boldsymbol{b}}_{1\times2}$ and $\underline{Y}_{\mathrm{gdc}}$ in (12) can be written as

$$\begin{aligned}\underline{\boldsymbol{b}}_{1\times2} &= \underline{G}_{\mathrm{d}}\left[\boldsymbol{M}^{\mathrm{T}}_{\mathrm{g1}} + \boldsymbol{I}^{\mathrm{T}}_{\mathrm{g1}}\left(\underline{\boldsymbol{G}}_{\mathrm{gi}} + \boldsymbol{K}_{\mathrm{gd}}\right)\right]\underline{\boldsymbol{Y}}_{\mathrm{gsc}} \\ &\quad + \underline{G}_{\mathrm{d}}\boldsymbol{I}^{\mathrm{T}}_{\mathrm{g1}}\left[\underline{\boldsymbol{G}}^{\mathrm{m}}_{\mathrm{PLL}} + \left(\underline{\boldsymbol{G}}_{\mathrm{gi}} + \boldsymbol{K}_{\mathrm{gd}}\right)\underline{\boldsymbol{G}}^{\mathrm{i}}_{\mathrm{PLL}} + \underline{\boldsymbol{G}}^{\mathrm{u}}_{\mathrm{PLL}}\right] \\ \underline{Y}_{\mathrm{gdc}} &= \underline{G}_{\mathrm{d}}\left\{-\boldsymbol{I}^{\mathrm{T}}_{\mathrm{g1}}\underline{\boldsymbol{G}}_{\mathrm{gi}}\underline{\boldsymbol{h}}_{\mathrm{vdc}}\right. \\ &\quad \left. + \left[\boldsymbol{M}^{\mathrm{T}}_{\mathrm{g1}} + \boldsymbol{I}^{\mathrm{T}}_{\mathrm{g1}}\left(\underline{\boldsymbol{G}}_{\mathrm{gi}} + \boldsymbol{K}_{\mathrm{gd}}\right)\right]\underline{\boldsymbol{a}}_{2\times1}\right\}\end{aligned} \tag{A2}$$

TABLE 1. Parameters of the simulated 5 MW DFIG-based wind turbine.

Description	Values
Rated Voltage / Power	950 V / 5 MW
DFIG generator (pu)	$R_s = 0.023,\ L_{\sigma s} = 0.18,\ R_r = 0.016,\ L_{\sigma r} = 0.16,\ L_m = 2.9$
GSC side reactor (pu)	$R_p = 0.003,\ L_p = 0.3$
Current controllers	GSC: $K_{gp} = 0.28,\ K_{gi} = 5$, RSC: $K_{rp} = 0.15,\ K_{ri} = 2$
DC voltage regulator	$K_{dcp} = 8,\ K_{dci} = 400$
DC bus parameters	capacitor 30000 μF , nominal voltage 1900 V
Speed regulator	$K_{sp} = 3,\ K_{si} = 0.6$
Q regulator	$K_{qp} = 0.03,\ K_{qi} = 1$
Terminal filter	400 kvar , Q=50 (Quality factor)
Step-up transformer	5.5 MVA, 0.95 /33 kV, $u_k = 5\%,\ u_r = 0.17\%,\ R_m = 500$ (pu), $L_m =$ inf
Sampling period	$T_s = 5\ \mu s$
Switching frequency	2 kHz
PLL	$K_{pp} = 16,\ K_{pi} = 50$

TABLE 2. Parameters of collector cables.

Cross-section	Electrical Parameters per km	Section Length
150 mm^2	$R = 0.16\ \Omega, L = 0.41$ mH, $C = 0.21$ μF	1 km
240 mm^2	$R = 0.098\ \Omega, L = 0.38$ mH, $C = 0.24$ μF	1 km
500 mm^2	$R = 0.05\ \Omega, L = 0.34$ mH, $C = 0.32$ μF	1 km

TABLE 3. Parameters of the aggregated WT representing N_{wt} single WTs.

Rated Power: $5 \cdot N_{wt}$ MW	DC side capacitor: $30000 \cdot N_{wt}$ μF
Terminal filter: $400 \cdot N_{wt}$ kvar	Step-up transformer: $5.5 \cdot N_{wt}$ MVA
Other parameters are same with the parameters of a single WT	

Detailed expressions of $\underline{\boldsymbol{A}}$ and $\underline{\boldsymbol{B}}$ in (19) can be written as

$$\begin{aligned}\underline{\boldsymbol{A}} &= \underline{G}_d U_{dc0}\left[\underline{\boldsymbol{G}}^{m}_{wtr} - \left(\underline{\boldsymbol{G}}_{ri} - \boldsymbol{K}_{rd} - \underline{\boldsymbol{G}}_{ri}\underline{\boldsymbol{G}}_{pq1}\right)\underline{\boldsymbol{G}}^{i}_{wtr}\right]\underline{\boldsymbol{Z}}_{sr}^{-1}\underline{\boldsymbol{Z}}_{ss} \\ &\quad - \underline{G}_d U_{dc0}\underline{\boldsymbol{G}}_{ri}\underline{\boldsymbol{G}}_{var2} + \underline{\boldsymbol{Z}}_{rs} - \underline{\boldsymbol{Z}}_{rr}\underline{\boldsymbol{Z}}_{sr}^{-1}\underline{\boldsymbol{Z}}_{ss} \\ \underline{\boldsymbol{B}} &= \underline{\boldsymbol{G}}^{rm}_{PLL} - \left(\underline{\boldsymbol{G}}_{ri} - \boldsymbol{K}_{rd} - \underline{\boldsymbol{G}}_{ri}\underline{\boldsymbol{G}}_{pq1}\right)\underline{\boldsymbol{G}}^{ri}_{PLL} \\ &\quad + \left(\boldsymbol{K}_{us} + \underline{\boldsymbol{G}}_{ri}\underline{\boldsymbol{G}}_{var1}\right)\underline{\boldsymbol{G}}^{u}_{PLL} + \underline{\boldsymbol{G}}_{ri}\underline{\boldsymbol{G}}_{var2}\underline{\boldsymbol{G}}^{si}_{PLL} \\ &\quad + \left(\underline{\boldsymbol{G}}^{m}_{wtr} - \left(\underline{\boldsymbol{G}}_{ri} - \boldsymbol{K}_{rd} - \underline{\boldsymbol{G}}_{ri}\underline{\boldsymbol{G}}_{wt}\right)\right)\underline{\boldsymbol{G}}^{i}_{wtr}\underline{\boldsymbol{Z}}_{sr}^{-1} \end{aligned} \tag{A3}$$

Detailed expressions of $\underline{\boldsymbol{d}}_{1\times 2}$ and $\underline{Y}_{rdc}$ in (21) can be written as

$$\begin{aligned}\underline{\boldsymbol{d}}_{1\times 2} &= \underline{G}_d\left[\boldsymbol{M}^{T}_{r1} + \boldsymbol{I}^{T}_{r1}\underline{\boldsymbol{G}}^{m}_{wtr} - \boldsymbol{I}^{T}_{r1}\left(\underline{\boldsymbol{G}}_{ri} - \boldsymbol{K}_{rd}\right.\right. \\ &\quad \left.\left. - \underline{\boldsymbol{G}}_{ri}\underline{\boldsymbol{G}}_{pq1}\right)\underline{\boldsymbol{G}}^{i}_{wtr}\right]\cdot\left(\underline{\boldsymbol{Z}}_{sr}^{-1} - \underline{\boldsymbol{Z}}_{sr}^{-1}\underline{\boldsymbol{Z}}_{ss}\underline{\boldsymbol{Y}}_{rsc}\right) \\ &\quad - \underline{G}_d\boldsymbol{I}^{T}_{r1}\left(\underline{\boldsymbol{G}}_{ri} - \boldsymbol{K}_{rd} - \underline{\boldsymbol{G}}_{ri}\underline{\boldsymbol{G}}_{pq1}\right)\underline{\boldsymbol{G}}^{ri}_{PLL} + \underline{G}_d\boldsymbol{I}^{T}_{r1}\underline{\boldsymbol{G}}^{rm}_{PLL} \\ &\quad + \underline{G}_d\boldsymbol{I}^{T}_{r1}\left(\underline{\boldsymbol{K}}_{us} + \underline{\boldsymbol{G}}_{ri}\underline{\boldsymbol{G}}_{var1}\right)\underline{\boldsymbol{G}}^{u}_{PLL} \\ &\quad + \underline{G}_d\boldsymbol{I}^{T}_{r1}\underline{\boldsymbol{G}}_{ri}\underline{\boldsymbol{G}}_{var2}\underline{\boldsymbol{G}}^{si}_{PLL} + \underline{G}_d\boldsymbol{I}^{T}_{r1}\underline{\boldsymbol{G}}_{ri}\underline{\boldsymbol{G}}_{var2}\underline{\boldsymbol{Y}}_{rsc} \\ \underline{Y}_{rdc} &= -\underline{G}_d\left[\boldsymbol{M}^{T}_{r1} + \boldsymbol{I}^{T}_{r1}\underline{\boldsymbol{G}}^{m}_{wtr} - \boldsymbol{I}^{T}_{r1}\left(\underline{\boldsymbol{G}}_{ri} - \boldsymbol{K}_{rd}\right.\right. \\ &\quad \left.\left. - \underline{\boldsymbol{G}}_{ri}\underline{\boldsymbol{G}}_{pq1}\right)\underline{\boldsymbol{G}}^{i}_{wtr}\right]\underline{\boldsymbol{Z}}_{sr}^{-1}\underline{\boldsymbol{Z}}_{ss}\boldsymbol{c}_{2\times 1} \\ &\quad + \underline{G}_d\boldsymbol{I}^{T}_{r1}\underline{\boldsymbol{G}}_{ri}\underline{\boldsymbol{G}}_{var2}\boldsymbol{c}_{2\times 1} \end{aligned} \tag{A4}$$

TABLE 4. Parameters of the aggregated cable models.

Aggregated cable items	Number of subsections	After-aggregation parameters (R in Ω, L in mH and C in μF)
Array 1 or 2	4	$R = 0.203,\ L = 0.722,\ C = 0.9$
Array 3, 4, 5 or 6	8	$R = 0.187,\ L = 1.105,\ C = 2.18$
MV collector system	40	$R = 0.034,\ L = 0.191,\ C = 10.52$

B. PARAMETERS OF MV COLLECTOR SYSTEM

See Tables 1–2.

C. PARAMETERS OF THE AGGREGATED MODEL OF MV COLLECTOR SYSTEM

See Tables 3–4.

REFERENCES

[1] *IEEE Recommended Practice and Requirements for Harmonic Control in Electric Power Systems*, IEEE Std 519-2014 (Revision IEEE Std 519-1992), Jun. 2014, pp. 1–29.

[2] Y. Zhang, C. Klabunde, and M. Wolter, "Study of resonance issues between DFIG-based offshore wind farm and HVDC transmission," *Electr. Power Sys. Res.*, vol. 190, Jan. 2021, Art. no. 106767.

[3] C. Buchhagen, C. Rauscher, A. Menze, and J. Jung, "BorWin1—First experiences with harmonic interactions in converter dominated grids," in *Proc. Int. ETG Congr.*, Nov. 2015, pp. 1–7.

[4] C. Buchhagen, M. Greve, A. Menze, and J. Jung, "Harmonic stability-practical experience of a TSO," in *Proc. 15th Wind Integr. Workshop*, 2016, pp. 1–6.

[5] M. Brendel and G. Traufetter, "Knall auf hoher See," *Der Spiegel*, vol. 35, pp. 71–72, Aug. 2014.

[6] M. Ndreko, C. Petino, and W. Winter, "High penetration of inverter based generation in the power system: A discussion on stability challenges and a roadmap for R&D," in *Proc. 4th Int. Hybrid Power Syst. Workshop, Crete*, 2019, pp. 1–7.

[7] X. Xie, X. Zhang, H. Liu, H. Liu, Y. Li, and C. Zhang, "Characteristic analysis of subsynchronous resonance in practical wind farms connected to series-compensated transmissions," *IEEE Trans. Energy Convers.*, vol. 32, no. 3, pp. 1117–1126, Sep. 2017.

[8] Z. Miao, "Impedance-Model-Based SSR analysis for type 3 wind generator and series-compensated network," *IEEE Trans. Energy Convers.*, vol. 27, no. 4, pp. 984–991, Dec. 2012.

[9] Y. Song, X. Wang, and F. Blaabjerg, "Impedance-based high-frequency resonance analysis of DFIG system in weak grids," *IEEE Trans. Power Electron.*, vol. 32, no. 5, pp. 3536–3548, May 2017.

[10] Y. Song, E. Ebrahimzadeh, and F. Blaabjerg, "Analysis of high-frequency resonance in DFIG-based offshore wind farm via long transmission cable," *IEEE Trans. Energy Convers.*, vol. 33, no. 3, pp. 1036–1046, Sep. 2018.

[11] Y. Zhang, C. Klabunde, and M. Wolter, "Harmonic filtering in DFIG-based offshore wind farm through resonance damping," in *Proc. IEEE PES Innov. Smart Grid Technol. Eur. (ISGT-Eur.)*, Sep. 2019, pp. 1–5.

[12] M. Amin and M. Molinas, "Understanding the origin of oscillatory phenomena observed between wind farms and HVdc systems," *IEEE J. Emerg. Sel. Topics Power Electron.*, vol. 5, no. 1, pp. 378–392, Mar. 2017.

[13] J. Lyu, X. Zhang, X. Cai, and M. Molinas, "Harmonic state-space based small-signal impedance modeling of a modular multilevel converter with consideration of internal harmonic dynamics," *IEEE Trans. Power Electron.*, vol. 34, no. 3, pp. 2134–2148, Mar. 2019, doi: 10.1109/TPEL.2018.2842682.

[14] Y. Zhang, C. Klabunde, and M. Wolter, "Harmonic resonance analysis for DFIG-based offshore wind farm with VSC-HVDC connection," in *Proc. IEEE Milan PowerTech*, Jun. 2019, pp. 1–6, doi: 10.1109/PTC.2019.8810495.

[15] H. Zong, J. Lyu, C. Zhang, X. Cai, M. Molinas, and F. Rao, "MIMO impedance based stability analysis of DFIG-based wind farm with MMC-HVDC in modifed sequence domain," in *Proc. 8th Renew. Power Gener. Conf. (RPG)*, Shanghai, China, 2019, pp. 1–7, doi: 10.1049/cp.2019.0652.
[16] H. Zong, C. Zhang, J. Lyu, X. Cai, M. Molinas, and F. Rao, "Generalized MIMO sequence impedance modeling and stability analysis of MMC-HVDC with wind farm considering frequency couplings," *IEEE Access*, vol. 8, pp. 55602–55618, 2020, doi: 10.1109/ACCESS.2020.2981177.
[17] I. Vieto and J. Sun, "Refined small-signal sequence impedance models of type-III wind turbines," in *Proc. IEEE Energy Convers. Congr. Expo. (ECCE)*, Portland, OR, USA, Sep. 2018, pp. 2242–2249, doi: 10.1109/ECCE.2018.8558477.
[18] Y. Xu, H. Nian, T. Wang, L. Chen, and T. Zheng, "Frequency coupling characteristic modeling and stability analysis of doubly fed induction generator," *IEEE Trans. Energy Convers.*, vol. 33, no. 3, pp. 1475–1486, Sep. 2018, doi: 10.1109/TEC.2018.2800043.
[19] H. Nian, Y. Xu, L. Chen, and M. Zhu, "Modeling and analysis of DC-link dynamics in DFIG system with an indicator function," *IEEE Access*, vol. 7, pp. 125401–125412, 2019, doi: 10.1109/ACCESS.2019.2938796.
[20] C. Zhang, X. Cai, M. Molinas, and A. Rygg, "Frequency-domain modelling and stability analysis of a DFIG-based wind energy conversion system under non-compensated AC grids: Impedance modelling effects and consequences on stability," *IET Power Electron.*, vol. 12, no. 4, pp. 907–914, Apr. 2019, doi: 10.1049/iet-pel.2018.5527.
[21] X. Chen and Z. Liu, "Impedance modeling and stability analysis of the converters in a double-fed induction generator (DFIG)-based system," *Energies*, vol. 12, no. 13, p. 2500, Jun. 2019.
[22] K. Sun, W. Yao, J. Fang, X. Ai, J. Wen, and S. Cheng, "Impedance modeling and stability analysis of grid-connected DFIG-based wind farm with a VSC-HVDC," *IEEE J. Emerg. Sel. Topics Power Electron.*, vol. 8, no. 2, pp. 1375–1390, Jun. 2020, doi: 10.1109/JESTPE.2019.2901747.
[23] A. Rygg, M. Molinas, C. Zhang, and X. Cai, "A modified sequence-domain impedance definition and its equivalence to the dq-domain impedance definition for the stability analysis of AC power electronic systems," *IEEE J. Emerg. Sel. Topics Power Electron.*, vol. 4, no. 4, pp. 1383–1396, Dec. 2016.
[24] N. W. Miller, J. J. Sanchez-Gasca, W. W. Price, and R. W. Delmerico, "Dynamic modeling of GE 1.5 and 3.6 MW wind turbine-generators for stability simulations," in *Proc. IEEE Power Eng. Soc. Gen. Meeting*, vol. 3, Toronto, ON, Canada, 2003, pp. 1977–1983.
[25] B. Wu, Y. Lang, N. Zargari, and S. Kouro, *Power Conversion and Control of Wind Energy Systems*. Hoboken, NJ, USA: Wiley, 2011.
[26] E. Muljadi, C. P. Butterfield, A. Ellis, J. Mechenbier, J. Hochheimer, R. Young, N. Miller, R. Delmerico, R. Zavadil, and J. C. Smith, "Equivalencing the collector system of a large wind power plant," in *Proc. IEEE Power Eng. Soc. Gen. Meeting*, Jun. 2006, p. 9.
[27] H. Kocewiak, "Harmonics in large offshore wind farms," Ph.D. dissertation, Dept. Energy Technol., Aalborg Univ., Aalborg, Denmark, 2012.
[28] B. Wen, D. Boroyevich, R. Burgos, P. Mattavelli, and Z. Shen, "Analysis of D-Q small-signal impedance of grid-tied inverters," *IEEE Trans. Power Electron.*, vol. 31, no. 1, pp. 675–687, Jan. 2016.
[29] W. Xu, "Component modeling issues for power quality assessment," *IEEE Power Eng. Rev.*, vol. 21, no. 11, pp. 12–17, Nov. 2001.
[30] *XLPE Submarine Cable Systems, Attachment to XLPE Land Cable Systems—User's Guide, Revision 5*, ABB, Zürich, Switzerland, 2007.
[31] J. Lyu, X. Cai, and M. Molinas, "Optimal design of controller parameters for improving the stability of MMC-HVDC for wind farm integration," *IEEE J. Emerg. Sel. Topics Power Electron.*, vol. 6, no. 1, pp. 40–53, Mar. 2018.
[32] X. Liu and A. Lindemann, "Control of VSC-HVDC connected offshore windfarms for providing synthetic inertia," *IEEE J. Emerg. Sel. Topics Power Electron.*, vol. 6, no. 3, pp. 1407–1417, Sep. 2018.
[33] I. Vieto and J. Sun, "Damping of subsynchronous resonance involving type-III wind turbines," in *Proc. IEEE 16th Workshop Control Model. for Power Electron. (COMPEL)*, Vancouver, BC, Canada, Jul. 2015, pp. 1–8, doi: 10.1109/COMPEL.2015.7236515.
[34] W. Liu, X. Xie, X. Zhang, and X. Li, "Frequency-coupling admittance modeling of converter-based wind turbine generators and the control-hardware-in-the-loop validation," *IEEE Trans. Energy Convers.*, vol. 35, no. 1, pp. 425–433, Mar. 2020.
[35] G. Francis, R. Burgos, D. Boroyevich, F. Wang, and K. Karimi, "An algorithm and implementation system for measuring impedance in the D-Q domain," in *Proc. IEEE Energy Convers. Congr. Expo.*, Phoenix, AZ, USA, Sep. 2011, pp. 3221–3228.
[36] S. Shah, P. Koralewicz, V. Gevorgian, R. Wallen, K. Jha, D. Mashtare, R. Burra, and L. Parsa, "Large-signal impedance-based modeling and mitigation of resonance of converter-grid systems," *IEEE Trans. Sustain. Energy*, vol. 10, no. 3, pp. 1439–1449, Jul. 2019.

YONGGANG ZHANG (Graduate Student Member, IEEE) was born in Tangshan, China, in 1983. He received the B.S. degree in electrical engineering from Chang'an University, Xi'an, China, in 2007, and the M.S. degree in electrical engineering from the University of Duisburg–Essen, Germany, in 2010. He is currently pursuing the Ph.D. degree in electrical engineering with Otto von Guericke University Magdeburg.

He was with NARI from 2011 to 2012 and China Electric Power Research Institute from 2012 to 2016, both with the Department of Power Automation. His current research interests include modeling and control of voltage-source converters, harmonic stability and power quality, and passive and active filters.

CHRISTIAN KLABUNDE (Member, IEEE) was born in Magdeburg, Germany, in 1991. He received the B.S. and M.S. degrees from Otto von Guericke University Magdeburg (OVGU), in 2013 and 2014, respectively, where he is currently pursuing the Ph.D. degree in electrical engineering.

His current research interests include the development of new grid planning and operation concepts, for example, time series-based redispatch optimization and voltage control.

MARTIN WOLTER (Senior Member, IEEE) was born in Hannover, Germany, in 1981. He received the Diploma, Ph.D., and Habilitation degrees from Leibniz University, Hannover, in 2006, 2008, and 2012, respectively.

From 2011 to 2015, he was the Head of the System Operation Concept Development Team, 50Hertz Transmission GmbH, Germany. Since 2015, he has been the Head of the Chair Electric Power Networks and Renewable Energy, Otto von Guericke University Magdeburg. His research interests include the modeling and simulation of interconnected electric power systems and the development of planning and operation strategies as well as multi-agent systems.